Monthly Notices of the ROYAL ASTRONOMICAL SOCIETY

MNRAS **524,** 5548–5565 (2023) https://doi.org/10.1093/mnras/stad2135
Advance Access publication 2023 July 18

Gaia21bty: An EXor light curve exhibiting a FUor spectrum

Michał Siwak [1,2★] Lynne A. Hillenbrand,[3] Ágnes Kóspál,[1,2,4,5] Péter Ábrahám,[1,2,4] Teresa Giannini,[6] Kishalay De,[7] Attila Moór,[1,2] Máté Szilágyi [1,2,4] Jan Janík [8] Chris Koen,[9] Sunkyung Park [1,2] Zsófia Nagy [1,2] Fernando Cruz-Sáenz de Miera [1,2] Eleonora Fiorellino,[1,2,10] Gábor Marton [1,2] Mária Kun [1,2] Philip W. Lucas [11] Andrzej Udalski[12] and Zsófia Marianna Szabó[1,2,13,14]

[1]*Konkoly Observatory, Research Centre for Astronomy and Earth Sciences, Eötvös Loránd Research Network (ELKH), Hungarian Academy of Sciences, Konkoly-Thege Miklós út 15–17, H-1121 Budapest, Hungary*
[2]*CSFK, MTA Centre of Excellence, Konkoly Thege Miklós út 15–17, H-1121 Budapest, Hungary*
[3]*Department of Astronomy, California Institute of Technology, Pasadena, CA 91125, USA*
[4]*Institute of Physics, ELTE Eötvös Loránd University, Pázmány Péter sétány 1/A, H-1117 Budapest, Hungary*
[5]*Max Planck Institute for Astronomy, Königstuhl 17, D-69117 Heidelberg, Germany*
[6]*INAF-Osservatorio Astronomico di Roma, via di Frascati 33, I-00040 Monte Porzio Catone, Italy*
[7]*Kavli Institute for Astrophysics and Space Research, Massachusetts Institute of Technology, Cambridge, MA 02139, USA*
[8]*Department of Theoretical Physics and Astrophysics, Masaryk University, Kotlářská 2, Brno, CZ-611 37, Czech Republic*
[9]*Department of Statistics, University of the Western Cape, Private Bag X17, Bellville, 7535 Cape, South Africa*
[10]*INAF-Osservatorio Astronomico di Capodimonte, via Moiariello 16, I-80131 Napoli, Italy*
[11]*Centre for Astrophysics, University of Hertfordshire, College Lane, Hatfield AL10 9AB, UK*
[12]*Astronomical Observatory, University of Warsaw, Al. Ujazdowskie 4, PL-00-478 Warszawa, Poland*
[13]*Max-Planck-Institut für Radioastronomie, Auf dem Hügel 69, D-53121 Bonn, Germany*
[14]*Scottish Universities Physics Alliance (SUPA), School of Physics and Astronomy, University of St Andrews, North Haugh, St Andrews KY16 9SS, UK*

Accepted 2023 July 13. Received 2023 July 13; in original form 2023 April 7

ABSTRACT

Gaia21bty, a pre-main-sequence star that previously had shown aperiodic dips in its light curve, underwent a considerable $\Delta G \approx 2.9$ mag brightening that occurred over a few months between 2020 October and 2021 February. The *Gaia* light curve shows that the star remained near maximum brightness for about 4–6 months, and then started slowly fading over the next 2 yr, with at least three superimposed ∼1 mag sudden rebrightening events. Whereas the amplitude and duration of the maximum is typical for EX Lupi-type stars, optical and near-infrared spectra obtained at the maximum are dominated by features which are typical for FU Ori-type stars (FUors). Modelling of the accretion disc at the maximum indicates that the disc bolometric luminosity is 43 $L_\odot$ and the mass accretion rate is 2.5×10^{-5} $M_\odot\,yr^{-1}$, which are typical values for FUors even considering the large uncertainty in the distance ($1.7^{+0.8}_{-0.4}$ kpc). Further monitoring is necessary to understand the cause of the quick brightness decline, the rebrightening, and the other post-outburst light changes, as our multicolour photometric data suggest that they could be caused by a long and discontinuous obscuration event. We speculate that the outburst might have induced large-scale inhomogeneous dust condensations in the line of sight leading to such phenomena, whilst the FUor outburst continues behind the opaque screen.

Key words: accretion, accretion discs – stars: formation – stars: pre-main-sequence – stars: variables: T Tauri, Herbig Ae/Be.

1 INTRODUCTION

FU Ori-type stars (FUors) were recognized by Herbig (1977) as classical T Tauri-type stars (CTTS) undergoing enhanced disc-matter accretion for a few decades or longer. In addition to FUors, Herbig (1989) established the group of EX Lupi-type stars (EXors), showing less dramatic eruptive events lasting considerably shorter, but re-appearing on the time-scale of a few—a dozen of years. This bimodal classification was recently blurred upon the discovery of eruptive stars showing the properties of both FUors and EXors (Audard et al. 2014), e.g. V1647 Ori (Andrews, Rothberg & Simon 2004; Muzerolle et al. 2005; Acosta-Pulido et al. 2007) and V899 Mon (Ninan et al. 2015; Park et al. 2021). A recent summary of the enhanced accretion process across the whole range of pre-main-sequence (PMS) evolutionary stages and an attempt of unification of the zoo of accompanying photometric and spectroscopic features were presented by Fischer et al. (2022), and in a modest form by Contreras Peña et al. (2023).

Studies show also that eruptive events are much more common for Class I than Class II objects (Contreras Pena, Naylor & Morrell 2019; Guo et al. 2021; Fiorellino et al. 2023). According to e.g. Contreras Pena et al. (2019), all PMS stars should undergo at least a dozen of enhanced accretion events. This provides evidence for episodic accretion as the preferred model to explain the observed protostellar luminosity spread (Fischer et al. 2022). As enhanced accretion has a major impact on the inner disc temperature causing the expansion of the snow line of various volatiles (Cieza et al. 2016), multiwavelength

★ E-mail: michal.siwak@gmail.com

studies of outbursting young stars are also crucial for understanding the chemical evolution of protoplanetary discs and eventually also the composition and morphology of planetary systems, including our Solar system (Ábrahám et al. 2009, 2019; Hubbard 2017; Molyarova et al. 2018; Wiebe et al. 2019).

The recently most recognized list of about 40 young eruptive stars compiled by Audard et al. (2014) expands constantly. The ground-based All-Sky Automated Survey for Supernovae (Shappee et al. 2014; Kochanek et al. 2017) and the Zwicky Transient Facility (Masci et al. 2018, 2019) have discovered several outbursting stars. These include the EXor-/FUor-type object ASASSN-13db (Holoien et al. 2014; Sicilia-Aguilar et al. 2017), PTF14jg tentatively identified as a FUor-type object (Hillenbrand et al. 2019b), and so far unclassified strong but relatively short outburst in ASASSN-15qi (Herczeg et al. 2016). Discovery of 106 eruptive stars was reported in Contreras Peña et al. (2017a, b) during the VISTA Variables in the Via Lactea (VVV, Minniti et al. 2010) survey conducted in near-infrared (near-IR) bands.

The multipurpose *Gaia* spacecraft observes each part of the sky in broad-band filters several dozen times a year (Gaia Collaboration 2016). After a few years of continuous observations, *Gaia* became an effective tool for catching long-term brightness changes in various astronomical objects down to 21 mag. The community is notified about significant brightness variations via the *Gaia* Photometric Science Alert system (Hodgkin et al. 2021). There are many plausible mechanisms that could be responsible for the light variations observed in almost every single PMS star (see e.g. Siwak et al. 2019; Nagy et al. 2021; Fischer et al. 2022), but the most exciting are those resulting from substantially enhanced accretion.

Up until the time of writing, two outbursts observed by *Gaia* have been spectroscopically confirmed as FUors: Gaia17bpi (Hillenbrand et al. 2018) and Gaia18dvy (Szegedi-Elek et al. 2020), and four as EXors: Gaia18dvz (ESO-Hα99, Hodapp et al. 2019); Gaia20eae (originally found in ground-based data as PGIR20dwf by Hankins et al. 2020) and studied in detail by Ghosh et al. (2022) and Cruz-Sáenz de Miera et al. (2022); Gaia19fct (Miller et al. 2015; Park et al. 2022); and Gaia22dtk (Kuhn et al. 2022). Two other eruptive young stars identified from *Gaia* variability do not clearly fall either into the FUor or the EXor category but share properties of both; these are Gaia19ajj (Hillenbrand et al. 2019a) and Gaia19bey (Hodapp et al. 2020). In addition, the *Gaia* Alert system pointed our attention to the temporary fading in ESO-Hα 148 (since then also known as Gaia21elv), first analysed by Contreras Pena et al. (2019), but only now confirmed as a bona fide FUor (Nagy et al. 2023).

The object of interest here, Gaia21bty, was identified by the *Gaia* Science Alert system as a considerable 2.9 mag brightening of a very reddened star, 2MASS 17251419–3708140 or *Gaia* third Data Release (DR3) 5974356442830973056. The source is located about a degree to the west of υ Scorpii, in the Galactic mid-plane. Based on a machine-learning classification using *Wide-field Infrared Survey Explorer* (*WISE*) and *Gaia* DR2 data, Marton et al. (2016) gave a high probability (89.22 per cent) that this is a young stellar object (YSO). The star was also listed among YSO candidates by Kuhn et al. (2021). An initial analysis of the Gaia21bty spectrum, taken near its maximum brightness, indicated that it may be a FUor (Hillenbrand 2021).

Here, we present and analyse new and archival data for Gaia21bty and draw conclusions about its nature. In Section 2, we describe the reduction of the archival photometry, and our new spectroscopic and photometric data obtained during the outburst until early-2023. Then, in Section 3, we estimate spectral class, distance, and briefly characterize the environment of Gaia21bty. Results obtained from the analysis are presented and discussed in Section 4, and then summarized in Section 5.

2 OBSERVATIONS AND THE DATA REDUCTION

2.1 Optical and IR photometry

In order to characterize Gaia21bty in the pre-outburst stage, we collected archival optical and IR photometry from several sources (Section 2.1.1). Then, we obtained new photometry to characterize the outburst and post-outburst stages (Section 2.1.2).

2.1.1 Archival photometry

The earliest optical data were obtained on two close epochs, 2012 August 8 and 21, by the VST Photometric Hα Survey of the Southern Galactic Plane and Bulge (VPHAS+, Drew et al. 2014). The survey was conducted by means of the 2.6-m European Southern Observatory (ESO) VLT Survey Telescope (VST) at Cerro Paranal, equipped with the OMEGACAM and *ugriH*α filters. We collected calibrated fits images from the public ESO archive and unambiguously detected our source only in the *ri* filters. The star was only marginally detectable in the *H*α filter. We extracted the photometry using DAOPHOT procedures (Stetson 1987) distributed within the `astro-idl` library. To ensure optimal extraction, an aperture of 9 pixel (1.92 arcsec) was used for the target and four comparison stars. The inner and outer sky annuli were specifically adjusted for each star to enable accurate sky level calculation. We took the *ri* magnitudes of the comparison stars from the APASS9 catalogue (Henden et al. 2015,). The four comparison stars available on the same CCD chip as our target have bluer colour indices, but careful extrapolation enabled us to obtain approximate transformation to the Sloan system. We plot these results in Fig. 1a and show in Table 1. In the same figure (and also in Fig. 1b with IR data) we present *Gaia G*-band data, connected with lines to facilitate navigation.

Optical data were also gathered during a few epochs between 2016 August 11 and 2019 July 19 by the DECam Plane Survey (DECaPS, Schlafly et al. 2018). The survey was conducted by means of the Dark Energy Camera (DECam) equipped with the *grizY* filters, installed on the 4-m *Blanco* telescope at the Cerro Tololo Inter-American Observatory in Chile. We downloaded calibrated fits images from the survey's public archive and (for consistency with VPHAS+ and our future observations) extracted the photometry using the same apertures (in arcseconds) as for the VPHAS+ data. The *gri* magnitudes of the three-to-five (depending on saturation) comparison stars were taken from the APASS9 catalogue. To obtain the *z* and *Y* magnitudes, we plotted their broad-band spectral energy distribution (SED) using their APASS9 and 2MASS magnitudes (Cutri et al. 2003), and then used spline interpolation for the filters' effective wavelengths (Fig. 1a, Table 1). Note that Gaia21bty is marginally detectable in the *g* band (with 0.9 mag uncertainty), but only during one night.

Between 2016 March 2 and 2018 April 7, the star was observed by the Optical Gravitational Lensing Experiment (OGLE, Udalski, Szymański & Szymański 2015), conducted with the 1.3-m *Warsaw University Telescope* at the Las Campanas Observatory in Chile. The data were obtained using the third-generation OGLE-IV mosaic camera equipped with the interferometric *VI* filters manufactured by Asahi Spectra, but significant detection of Gaia21bty was possible

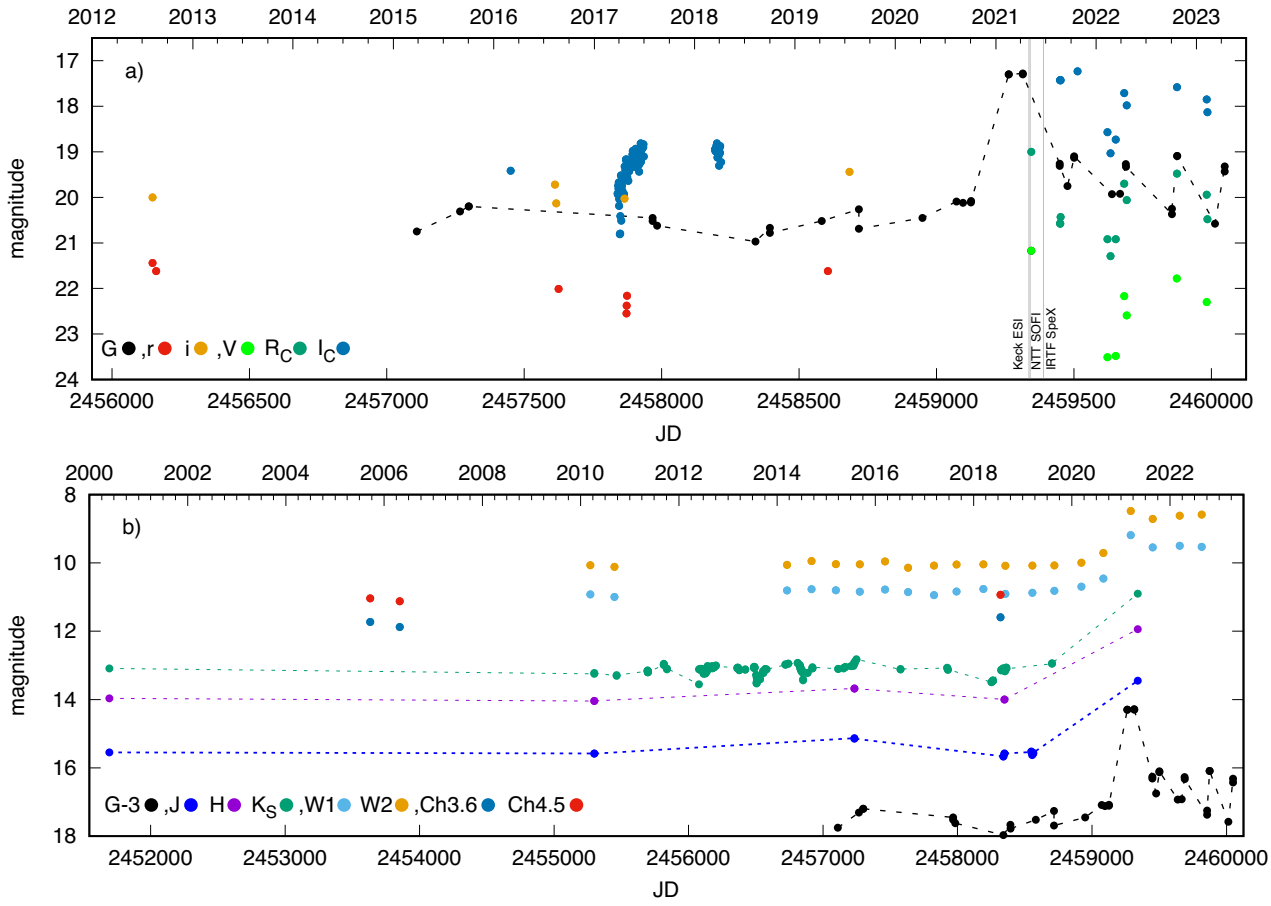

Figure 1. Optical (top panel) and IR (bottom panel) light curves of Gaia21bty. Moments of spectroscopic observations are indicated in the first plot. JHK_S pre-outburst observations were obtained by 2MASS and VVVX surveys, while *New Technology Telescope* (*NTT*) equipped with Son of ISAAC (SOFI) covered the maximum stage. Due to the nebulosity, the brightness in the *WISE* bands *W*1 (3.4 μm) and *W*2 (4.6 μm) is higher by about 1 mag than in the respective *Spitzer* 3.6 and 4.5 μm channels from 2018. *Gaia* light curve (shifted by 3 mag) is plotted again to facilitate the navigation. The error bars are comparable in size or smaller than the points, and are omitted for clarity. The comas in the legends are to separate photometric systems.

only for the *I* band ($\lambda_{\rm eff}$ = 793.2 nm). The photometry used in this paper (Figs 1a and 2) was extracted by means of the dedicated OGLE pipeline, as described in Udalski et al. (2015).

The first pre-outburst IR measurements in JHK_S filters used in this paper were obtained by the 2MASS survey on 2000 May 29 (Skrutskie et al. 2006). Then, between 2010 April 11 and 2019 August 6, the star was observed from the subsidiary summit of Cerro Paranal by the 4-m *Visible and Infrared Survey Telescope for Astronomy* (*VISTA*) equipped with the near-infrared imaging camera (VISTA IR Camera) and $ZYJHK_S$ filters (Sutherland et al. 2015). The data were obtained within the public ESO near-IR VVV survey and its extension (VVVX), which scanned the Milky Way bulge and the section of the mid-plane where star-formation rate (SFR) is supposed to be high (Minniti et al. 2010). The photometry (Figs 1b and 2) was extracted from a pre-release version of version 2 of the VVV Infrared Astrometric Catalogue (VIRAC2, see Smith et al. 2018, and Smith et al., in preparation). This provides time series photometry and five parameter absolute astrometric fits for sources using VVV/VVVX observations from 2010 to 2019. Individual sources were extracted by profile fitting photometry using DoPHOT (Schechter, Mateo & Saha 1993; Alonso-García et al. 2018), with improved photometric calibration. The astrometry is calibrated on to the *Gaia* DR3 reference frame.

To characterize the progenitor at longer wavelengths, we analysed data from the *Spitzer* (Werner et al. 2004) and the *WISE* (Wright et al. 2010) space telescopes. In the Spitzer Heritage Archive we found five observations that covered Gaia21bty obtained with the Infrared Array Camera (IRAC, Fazio et al. 2004), all as part of larger mapping projects. The first four measurements were performed during the cryogenic phase in 2005 and 2006. In two cases, Gaia21bty was observed at 3.6 and 5.8 μm, while in two other cases at 4.5 and 8 μm. The data corresponding to the latest epoch were obtained only in the 3.6 and 4.5 μm bands about 12 yr later, during the post-cryogenic (warm) phase. For photometry, we used the corrected basic calibrated data frames generated by the IRAC pipeline, all downloaded from the Spitzer Science Center. Aperture photometry was used to extract flux densities. The aperture radius was set to 2 pixels (∼2.″4), while the background was estimated in an annulus between radii of 2 and 6 pixels. The centroid of the source was determined by employing a first moment box centroider algorithm.[1] In addition to aperture correction, array-location and pixel phase correction were also performed. For

[1] https://irsa.ipac.caltech.edu/data/SPITZER/docs/dataanalysistools/tools/contributed/irac/box_centroider/

Table 1. Pre-outburst optical and IR photometry of Gaia21bty extracted from public-domain, calibrated images, gathered by different surveys.

JD	Filter	Mag	Unc	Survey
2456147.63402	*r*	21.44	0.08	VPHAS+
2456147.64006	*i*	20.00	0.05	VPHAS+
2456160.53970	*r*	21.62	0.10	VPHAS+
2457872.72827	*g*	24.87	0.92	DECaPS
2457624.67796	*r*	22.01	0.17	DECaPS
2457871.83275	*r*	22.55	0.20	DECaPS
2457872.72721	*r*	22.38	0.18	DECaPS
2457873.82431	*r*	22.16	0.18	DECaPS
2458604.83248	*r*	21.62	0.13	DECaPS
2457611.66478	*i*	19.72	0.15	DECaPS
2457616.69413	*i*	20.13	0.16	DECaPS
2457864.82449	*i*	20.03	0.16	DECaPS
2458683.60124	*i*	19.44	0.15	DECaPS
2457611.66545	*z*	17.67	0.13	DECaPS
2457616.69345	*z*	17.98	0.13	DECaPS
2457864.82518	*z*	18.00	0.12	DECaPS
2458683.60192	*z*	17.54	0.11	DECaPS
2457611.66612	*Y*	17.14	0.11	DECaPS
2457616.69277	*Y*	17.39	0.12	DECaPS
2457864.82587	*Y*	17.36	0.12	DECaPS
2458683.60262	*Y*	16.97	0.11	DECaPS
2453632.54274	[8.0]	10.461	0.172	GLIMPSE
2453632.54282	[4.5]	11.038	0.058	GLIMPSE
2453632.57065	[3.6]	11.731	0.053	GLIMPSE
2453632.57065	[5.8]	10.823	0.060	GLIMPSE
2453852.58020	[3.6]	11.879	0.085	GLIMPSE
2453852.58020	[5.8]	10.669	0.348	GLIMPSE
2453852.59760	[4.5]	11.121	0.085	GLIMPSE
2453852.59760	[8.0]	10.395	0.278	GLIMPSE
2458319.78485	[3.6]	11.591	0.026	GLIMPSE
2458319.79077	[4.5]	10.933	0.031	GLIMPSE

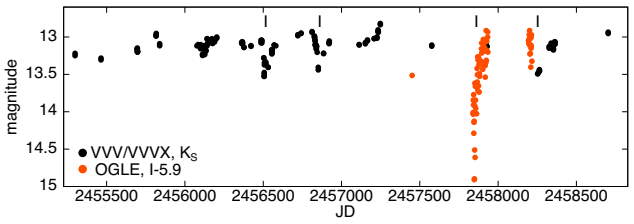

Figure 2. Enhanced view of the information in Fig. 1 showing the dips in *I* and K_S bands during the pre-outburst stage.

the latter two corrections, the `irac aphot corr` routine[2] was used, while the aperture correction factors were taken from the IRAC Instrument Handbook v3.01.[3] Except for one measurement where the target was observed only on one frame, we have multiple data points corresponding to the 2–6 frames available for the source. In the latter cases, the final flux densities and their uncertainties were obtained as the mean and the error of the mean of the individual values, respectively. The photometric data are shown in Table 1 and plotted in Fig. 1b. The quoted uncertainties are the quadratic sums of measurement and calibration errors, where the latter is adopted to be 2 per cent.

Gaia21bty was also observed with the Multiband Imaging Photometer for Spitzer (MIPS, Rieke et al. 2004). However, strong contamination from the nearby IR-nebula prevented us from obtaining accurate measurements in all MIPS bands, only a 3σ upper limit of 0.15 Jy could be estimated at 24 μm. This will have some repercussions when trying to classify our target (Section 3.1).

Two epochs, observed 6 months apart, were also collected during the fully cryogenic phase of *WISE* in *W*1, *W*2, *W*3, and *W*4 bands, centred at 3.4, 4.6, 12, and 22 μm, respectively. However, we noted that as in the case of *Spitzer*, no distinct point source is visible on top of the surrounding nebula in the *W*3 and *W*4 images, therefore, we rejected these catalogue measurements from further analyses. The NEOWISE mission continued to operate in *W*1 and *W*2 bands (Mainzer et al. 2011) providing long-term light curves covering the outburst. Starting from 2014, usually over a dozen individual measurements per filter were obtained during each of two (typically 2 d long) pointings towards our target. We downloaded individual catalogue measurements, removed obvious outliers, and computed averages and their standard deviations per each epoch. In spite of the nebulosity having impact on the real brightness level also in *W*1 and *W*2 bands, this is mostly a systematic effect, therefore the light curves still carry valuable information about the mid-IR brightness evolution.

2.1.2 *New photometry*

To characterize the outburst itself and the post-outburst behaviour, on 2021 May 10, we used the 3.58-m *NTT* of the ESO in La Silla, Chile. The ESO Faint Object Spectrograph and Camera version 2 (EFOSC2) camera equipped with BVR_C filters was used, but we detected our star in the *V*- and R_C-filter images only. The target remains undetected both on the three individual 40 s long, and on the combined (120 s in total) *B*-filter exposures. Then, in 2021 August and October, we used the 1-m *Elizabeth* telescope located at the South African Astronomical Observatory (SAAO). The telescope was equipped with the Sutherland High Speed Optical Camera (SHOC). We observed the star in the VR_CI_C filters, but we got no detection in the *V* band. This is due to the fact that contrary to our expectations, the source faded considerably by this time.

In 2022 February–2023 February, we observed the star on eight different nights using the *Danish* 1.54-m telescope at La Silla, Chile. We used the Danish Faint Object Spectrograph and Camera (DFOSC) equipped with Johnson–Cousins filters. The star remained undetected in the *B* filter either in any single 300 s individual exposures, or in the stacked (in total 30–50 min, depending on night) images. Positive detection was almost always achieved for the *V* band: The star remained undetected only during two nights with poor seeing conditions. The target was always well visible in the R_C- and I_C-band images.

We corrected our new raw images for bias, dark (when necessary), and flat-field using IRAF, and then applied DAOPHOT procedures. The magnitudes of the suitable comparison stars, four in the 4.1 × 4.1 arcmin field of view (FoV) on *NTT*, three in the 2.85 × 2.85 arcmin FoV on *Elizabeth*, and 34 in the 13.7 × 13.7 arcmin FoV of the *Danish* telescope, were obtained from the APASS9 and 2MASS catalogues (Cutri et al. 2003; Henden et al. 2015,). The missing R_C and I_C magnitudes were obtained by SED interpolation, like before. We used the same aperture size (in arcseconds) for the target and the (usually common) comparisons stars as for pre-outburst VPHAS+

[2]https://irsa.ipac.caltech.edu/data/SPITZER/docs/dataanalysistools/tools/contributed/irac/iracaphotcorr/

[3]https://irsa.ipac.caltech.edu/data/SPITZER/docs/irac/iracinstrumenthandbook/

Table 2. Outburst (top part) and post-outburst photometry of Gaia21bty extracted from images gathered during this work.

JD	Filter	Mag	Unc	Telescope/instrument
2459340.68850	J	13.449	0.044	*NTT*/SOFI
2459340.69101	H	11.937	0.029	*NTT*/SOFI
2459340.69352	K_S	10.902	0.028	*NTT*/SOFI
2459344.67628	V	21.17	0.12	*NTT*/EFOSC2
2459344.66854	R_C	19.00	0.05	*NTT*/EFOSC2
2459449.23811	R_C	20.57	0.32	*Elisabeth*/SHOC
2459449.24054	I_C	17.43	0.13	*Elisabeth*/SHOC
2459450.22208	R_C	20.58	0.15	*Elisabeth*/SHOC
2459450.21666	I_C	17.42	0.13	*Elisabeth*/SHOC
2459451.23182	R_C	20.43	0.11	*Elisabeth*/SHOC
2459451.22910	I_C	17.43	0.13	*Elisabeth*/SHOC
2459513.24948	I_C	17.23	0.16	*Elisabeth*/SHOC
2459621.86600	V	23.51	0.23	*Danish*/DFOSC
2459621.87700	R_C	20.92	0.08	*Danish*/DFOSC
2459621.88200	I_C	18.57	0.08	*Danish*/DFOSC
2459632.76602	R_C	21.29	0.15	*Danish*/DFOSC
2459632.77005	I_C	19.03	0.11	*Danish*/DFOSC
2459651.85932	V	23.48	0.27	*Danish*/DFOSC
2459651.82779	R_C	20.92	0.11	*Danish*/DFOSC
2459651.82959	I_C	18.73	0.09	*Danish*/DFOSC
2459682.86387	V	22.17	0.14	*Danish*/DFOSC
2459682.87036	R_C	19.70	0.07	*Danish*/DFOSC
2459682.90521	I_C	17.71	0.08	*Danish*/DFOSC
2459691.89099	V	22.59	0.25	*Danish*/DFOSC
2459691.88942	R_C	20.24	0.08	*Danish*/DFOSC
2459691.90696	I_C	17.98	0.08	*Danish*/DFOSC
2459874.49908	V	21.78	0.14	*Danish*/DFOSC
2459874.51736	R_C	19.48	0.06	*Danish*/DFOSC
2459874.53502	I_C	17.58	0.08	*Danish*/DFOSC
2459982.86807	V	22.30	0.15	*Danish*/DFOSC
2459982.83635	R_C	19.94	0.12	*Danish*/DFOSC
2459982.85189	I_C	17.85	0.09	*Danish*/DFOSC
2459985.87106	R_C	20.48	0.15	*Danish*/DFOSC
2459985.85622	I_C	18.13	0.07	*Danish*/DFOSC

and DECaPS data. We corrected our results for the colour extinction assuming the second-order colour extinction coefficients $\beta = -0.008$ both for R_C and I_C bands and -0.01 for the V-band (Siwak et al. 2018a, b). The small FoV of *NTT*/EFOSC2 and *Elisabeth*/SHOC cameras prevented us from observing comparison stars having colour indices similar to Gaia21bty to enable proper colour transformation, but we estimate that the lack of the full transformation to the standard system should not lead to systematic error higher than 0.15 mag. We plot the results in Fig. 1a and list the obtained magnitudes in Table 2.

On 2021 May 6 (at the maximum brightness) we obtained images in JHK_S filters with the IR spectrograph and imaging camera SOFI (Moorwood, Cuby & Lidman 1998), operating at the Nasmyth focus of *NTT*. The photometry was obtained using 20 comparison stars. They were carefully selected from the 2MASS catalogue (Cutri et al. 2003) bearing in mind both brightness and colour index similar to those of Gaia21bty. As the images were obtained in single position only and no other calibration images were available, we found and removed the *magnitude-coordinate* dependency by means of a two-dimensional quadratic function fit. No further dependency on colour index was found. We list the final results in Table 2 and plot in Fig. 1b. As expected, the NEOWISE mission continued as the outburst proceeded and contributed to post-outburst mid-IR light curve as well.

2.2 Optical and IR spectroscopy

Keck II equipped with the high throughput Echellette Spectrograph and Imager (ESI, Sheinis et al. 2002) was used to obtain the optical spectrum of Gaia21bty on 2021 May 1. ESI provided complete coverage from 390 to 1030 nm in a single 1800 s exposure. We used the cross-dispersed spectroscopy mode along the 0.5×20 arcsec slit, providing a resolving power up to $R = 8000$ (37 km s^{-1}). The spectra were processed in a standard way for bias and flat-field, and then wavelength-calibrated and heliocentric velocity-corrected by means of the dedicated MAKEE reduction package, written by Tom Barlow. As no telluric standard was observed, we removed the telluric lines using the MOLECFIT software (Kausch et al. 2015; Smette et al. 2015). We then scaled the observed spectrum to the absolute fluxes using nearly-simultaneous visual and IR photometry obtained at La Silla (Table 2). We show the final result in Fig. 3a.

Six days later, on 2021 May 6, we obtained the first near-IR spectrum by means of SOFI on *NTT*. We used the low-resolution blue and red grisms with GBF and GRF order sorting filters through the 0.6 arcsec wide slit, covering 0.95–1.64 and 1.53–2.52 μm with $R =$ 930 and 980, respectively. We reduced the spectra in IRAF according to the recipe given in the SOFI manual: First the sky level was approximately removed by subtraction of images obtained in A and B nod positions, and then the sky residuals were carefully removed during the spectrum extraction with the `apall` task. The Xenon lamp spectra and respective line lists provided for SOFI users were used for the wavelength calibration performed with the `(re)identify` and `dispcor` tasks. Then we removed atmospheric lines by means of the `telluric` task, in which we interactively scaled the normalized spectrum of the telluric standard star HD74194, obtained on similar airmass but 3 h earlier than the target. Finally we combined the cleaned images to form average 'blue' (0.95–1.64 μm) and 'red' (1.53–2.52 μm) spectra (Figs 3a and b).

The second near-IR spectrum was obtained on 2021 June 23 (i.e. 48 d after SOFI observations) by means of the NASA Infrared Telescope Facility (IRTF) equipped with SpeX (Rayner et al. 2003). SpeX is a medium-resolution IR spectrograph, which we used in the Short XD mode, providing 0.7–2.55 μm spectra with $R =$ 2000 through the 0.3×15 arcsec slit. The total integration time of six dithered spectra was 717 s. After the spectrum extraction by the dedicated pipeline, telluric correction was performed by division of the Gaia21bty spectrum by the spectrum of A0 star HIP 86098, located 2 deg from and observed immediately after the target at exactly the same 1.84 airmass. Then, the heliocentric velocity correction was applied. Both the SOFI and the SpeX spectra are plotted in Fig. 3b. One can note slightly higher flux obtained by SpeX than by SOFI. Due to the lack of simultaneous JHK_S photometry during the IRTF/SpeX observations and strong variability of the source, we cannot exclude that the enhanced flux seen by IRTF/SpeX relative to *NTT*/SOFI is real.

3 PROPERTIES OF GAIA21BTY

3.1 SED and classification of progenitor

We constructed the SED of Gaia21bty from the archival and new data (Section 2.1) obtained prior and during the outburst, as shown in Fig. 3c. Appropriate zero-points, necessary to transform observed magnitudes to flux units, were taken from the Spanish Virtual Observatory filter profile data base.[4]

[4] http://svo2.cab.inta-csic.es/theory/fps/

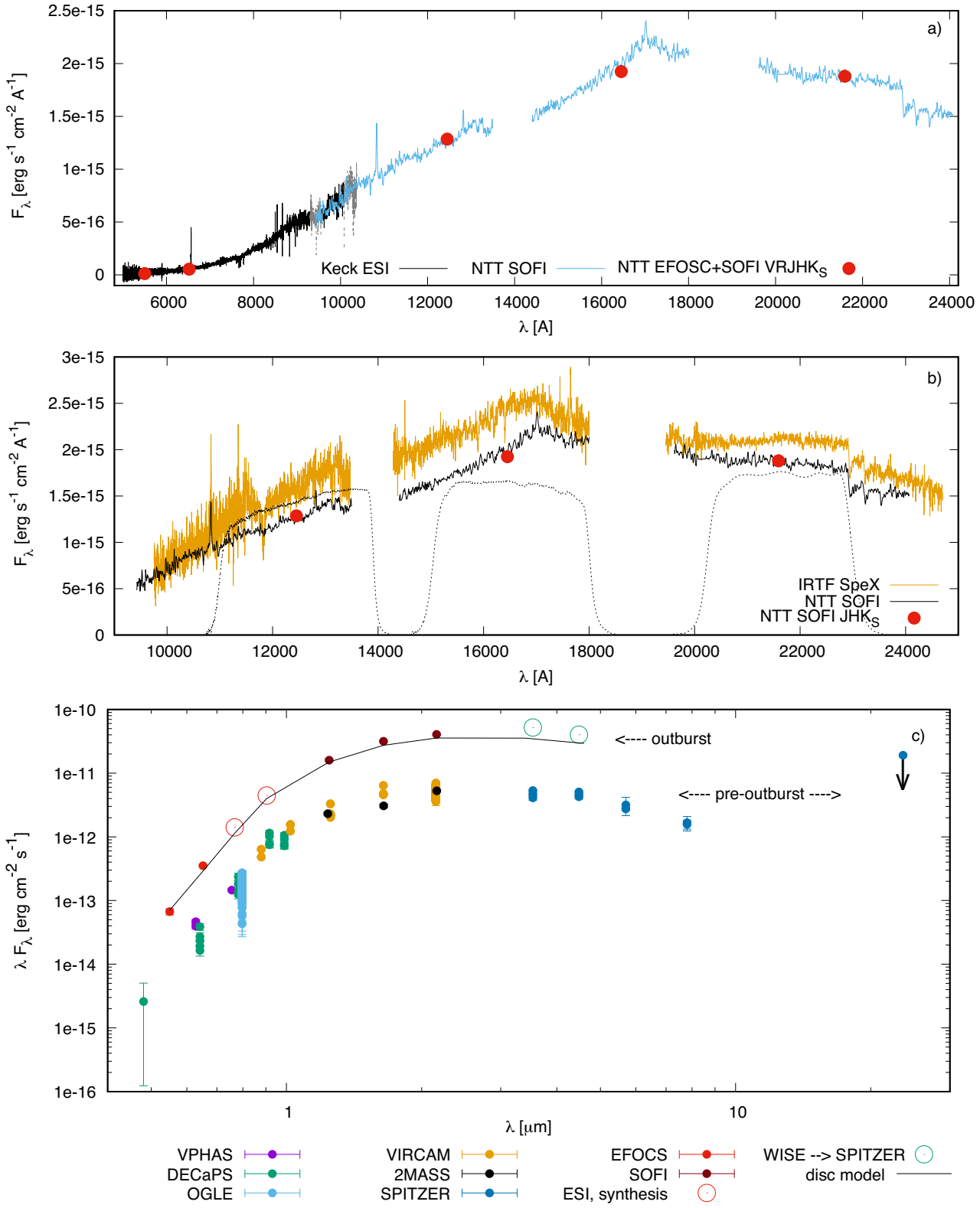

Figure 3. Optical (a) and IR (a, b) telluric-corrected spectra, scaled to fluxes. The noisy part below 5000 Å, and regions heavily contaminated by telluric lines, were marked by grey or removed. The profiles of SOFI's *JHK*$_S$ filters are plotted in panel b with dots for auxiliary purposes. Panel c shows the pre-outburst and the outburst SED of Gaia21bty. The Sloan *iz* magnitudes are synthetic, obtained from the optical spectrum integration. The NEOWISE *W*1 and *W*2 data from 2021 March 13 are transformed to *Spitzer* 3.6 and 4.5 μm bands, and indicated by large open circles to emphasize their larger beam. Result from our disc modelling is plotted as the dark line.

The pre-outburst SED is constructed from all data but *Gaia*, taken before 2020. Thus, some of them, like the OGLE *I*- and VVV/VVVX K_S-filter data, allow one visualizing the spread of energy received in the optical bands during the phenomena unrelated to the outburst, i.e. the obscuration events (Section 4.1). As mentioned in Section 2.1, due to the bright nebula and 5.4× larger pixel scale, the NEOWISE data (6.5 arcsec per pixel) indicate a much higher brightness of the target than those obtained by *Spitzer* (1.2 arcsec per pixel) at similar wavelengths. For this reason the NEOWISE measurements are omitted from the pre-outburst SED.

The spectral index α (Lada 1987) estimated between the *Spitzer* 4.5 and (the upper limit of) 24 μm fluxes (equation 7 in Kuhn et al. 2021) is ≤0.876, which suggests Class I, flat, or Class II evolutionary stage. However, Fig. 3c shows steady negative spectral index among 4.5, 5.8, and 8 μm, and not a deep silicate absorption at 8 μm. In these circumstances, the spectral index calculated from equation 9 in their paper, utilizing 8.0 μm magnitude, results in $\alpha = -1.7$. In addition, Fig. 7 suggests quite low near-IR excess fluxes above the main sequence. All the above supports Class II classification for our target.

The outburst fluxes were measured by *NTT* within 4 d, on 2021 May 6 in the JHK_S, and on May 10 in the VR_C filters. At that time the star was still in the maximum brightness, or just started the fade. Despite this uncertainty, throughout this paper we consequently assume that these data represent the maximum stage.

In addition to our data, thanks to the similarity between *Spitzer* 3.6 & 4.5 μm and NEOWISE *W*1 & *W*2 bands, we estimated the influence of the nebulosity on the latter photometry. For this purpose, we used the nearly-simultaneous measurements obtained in August 2018 (Fig. 1b). First, we converted the *W*1 and *W*2 magnitudes to fluxes in Jansky unit, then we aligned these light curves to match the respective *Spitzer*'s data, and converted back to magnitudes. The nebulosity-corrected NEOWISE measurements obtained on 2021 March 13 (certainly the outburst maximum) are $W1 = 9.318 \pm 0.031$ and $W2 = 8.619 \pm 0.033$ mag. We mark these points as open circles in Fig. 3c to indicate the indirect nature of these measurements. The same applies to the *i*- and *z*-band Sloan points, obtained from spectral synthesis of the Keck/ESI spectrum.

We will return to the pre-outburst and outburst SEDs analysis in Sections 4.5 and 4.6, after the interstellar extinction estimation.

3.2 Location and distance estimate

Gaia21bty ($\alpha_{J2000} = 17^{\rm h}\ 25^{\rm m}\ 14\overset{\rm s}{.}19$, $\delta_{J2000} = -37^{\circ}\ 08'\ 14\overset{''}{.}17$) is located in an optically dark region very close to the Milky Way mid-plane ($l = 350.79501^{\circ}$, $b = -0.84115^{\circ}$), in the southern part of Scorpius. This region was targeted by the *Spitzer* GLIMPSE II project, one of the goals of which was identification of mid-IR dust bubbles formed by hot O- and B-type young stars in massive star-forming regions, to trace recent and current star formation in the Milky Way (Churchwell et al. 2007). Yet, the MWP1G350770-008600S bubble adjacent to the dark region from which Gaia21bty emerged, was identified only later via the online citizen science website 'The Milky Way Project' (Simpson et al. 2012).

In the pre outburst stage, Gaia21bty was a relatively faint ($G = 20.364 \pm 0.027$ mag) and strongly reddened object (Section 2.1, Table 1), therefore there is no parallax in the *Gaia* DR3 (Gaia Collaboration 2022), nor in the earlier data releases. Gaia21bty has no proper motion in the *Gaia* DR3 catalogue. Therefore, we examined the comoving stars in the VIRAC2 catalogue. The proper motion of Gaia21bty in right ascension and declination was measured there as $pmra = 0.34 \pm 0.24$ mas yr^{-1} and $pmdec = -0.54 \pm 0.28$ mas yr^{-1},

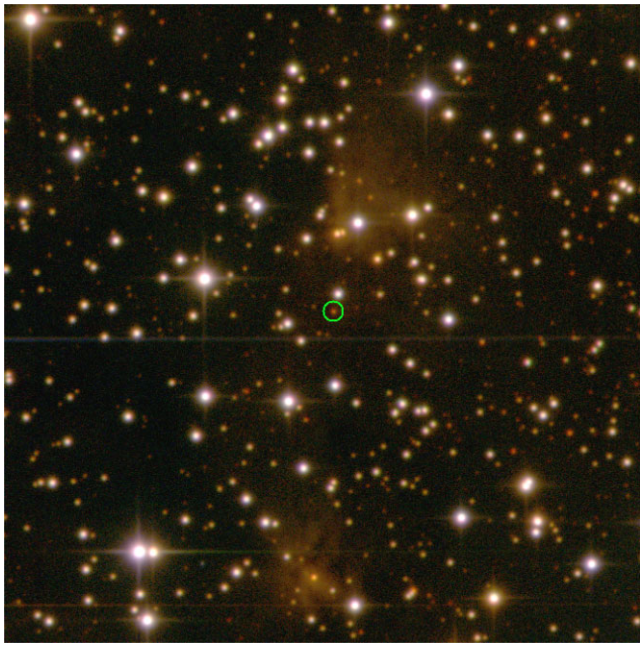

Figure 4. Composite *BVR* 4.5 × 4.5 arcmin image, obtained on 2022 April 12 by 1.54-m *Danish* telescope at La Silla. Gaia21bty, having then a brightness of $V = 22.17$ mag and $R_C = 19.70$ mag, is encircled with a 4 arcsec radius aperture. North is up, east is to the left.

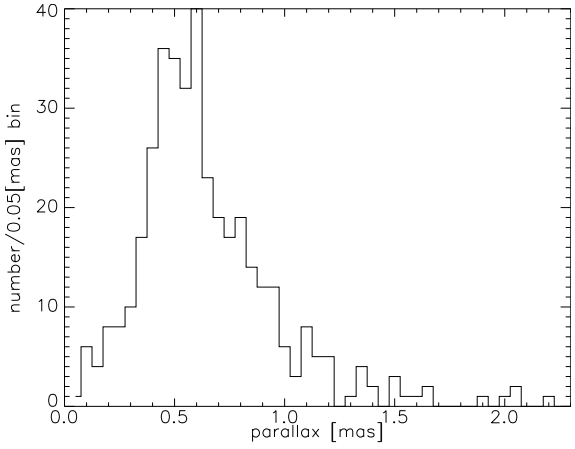

Figure 5. Distribution of parallaxes of red objects in the 4 arcmin vicinity of Gaia21bty.

respectively. Converting to Galactic coordinates, the proper motion in the Galactic longitude is $pml = 0.03 \pm 0.25$ mas yr^{-1} and in the Galactic latitude is $pmb = -0.64 \pm 0.27$ mas yr^{-1}. The essentially zero motion in the longitude direction indicates that it is probably within 5 kpc. This constrain is insufficient for our purposes. We thus searched for known YSOs in the vicinity of Gaia21bty with determined parallaxes.

Using the list of Kuhn et al. (2021), we found a dozen Class II YSOs in a 10 arcmin radius of Gaia21bty, out of which only one, SPICY 53729, has well-determined parallax 0.4847 ± 0.0636 mas, resulting in the distance $d \approx 2.06$ kpc. We also examined properties of YSO candidates from Marton et al. (2016, 2019) within the same 10 arcmin radius around Gaia21bty. Only three Class II objects with well-determined parallaxes were found in their first study, and the mean value is 0.49 ± 0.03 mas (2.04 kpc). In the 2019 catalogue,

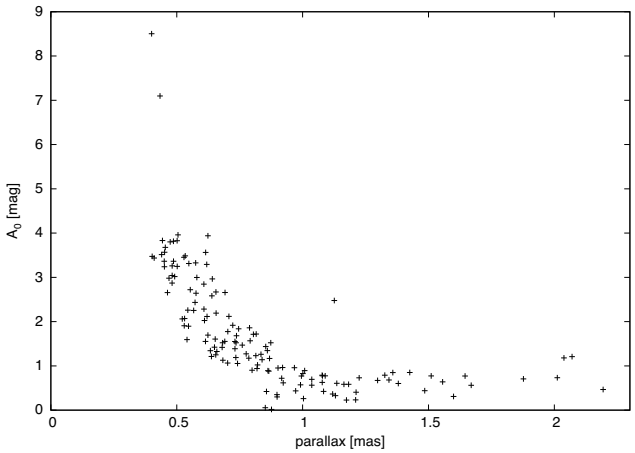

Figure 6. Interstellar extinction A_0 versus parallax, as obtained from *Gaia* DR3 for stars with well-determined parallaxes.

we found 74 stars for which the probability of being YSO is higher than 70 per cent. We removed the stars with negative parallaxes and considered only those having renormalized unit weight error *RUWE* ≤ 1.4 and parallaxes at least five times their errors. Based on 13 stars meeting these criteria, we obtained the median parallax 0.59 ± 0.20 mas, which corresponds to $d = 1.70^{+0.87}_{-0.43}$ kpc. This is in line with the Very Long Baseline Array (VLBA) results of Wu et al. (2014), who found that the typical distances to all nearby SFRs from the Sagittarius arm are $\leq$2 kpc (see the first few lines in table of their paper).

Furthermore, we checked whether red stars seen towards Gaia21bty could be members of Galactic spiral arms along the line of sight, specifically looking for those associated with the star-forming region related to the aforementioned bubble. Based again on the *Gaia* DR3 catalogue and considering only stars with *RUWE* ≤ 1.4, but now adding a selection for red colour index ($1.0 \leq B_P - R_P \leq 4.5$ mag), we analysed the parallaxes of objects localized within 4 arcmin radius around Gaia21bty. The distribution of parallaxes in 0.05 mas bins (Fig. 5) appears to be double-peaked with peaks at 0.6 mas (the formal median value of unbinned parallaxes equals to 0.588 mas, similarly as obtained above based on Marton et al. 2019), and at 0.45 mas.

Compiling our results obtained for YSOs in the same direction as Gaia21bty (Wu et al. 2014; Marton et al. 2016, 2019; Kuhn et al. 2021), we conclude that the distance to Gaia21bty is probably close to 1.7 kpc. It is certainly not shorter than 1.3 kpc, and not longer than 2.5 kpc. Throughout this paper we thus assume $d = 1.7^{+0.8}_{-0.4}$ kpc as the most likely value for the distance but will also use 1.3 and 2.5 kpc to derive lower and upper bounds for certain parameters.

The *Gaia* DR3 catalogue also offers a way to estimate the interstellar extinction by means of the A_0 parameter. It is computed for the monochromatic wavelength 541.4 nm by means of the blue and the red spectra obtained by the *Gaia* spacecraft. As such, A_0 is close to but not exactly the same as the extinction A_V in the Johnson V band (Creevey et al. 2023). Based on the sample of stars used for the histogram construction (Fig. 5), and imposing an extra constrain on the signal-to-noise ratio (S/N) of the parallax $\geq$7, we plot the A_0 versus parallax dependency in Fig. 6. Although the latest constraint severely affects the population of the more distant objects, the sample is sufficiently numerous to observe a clear trend. A_0 as high as 7–9 mag are obtained for stars near 2 kpc. If confirmed by more accurate methods of the A_V determination (see in Sections 4.4 and 4.6), such values would be in line with the very red colour index of Gaia21bty.

4 DATA ANALYSIS

4.1 Variability in the pre-outburst stage

Gaia21bty showed a few significant dips during the pre-outburst stage, as best evident in the most uniform and numerous data set gathered in the K_S filter by the VVV/VVVX survey. In general, the variability appears to show higher amplitudes at shorter wavelengths. We infer this mainly from the near-IR data, as shown in Fig. 2. This figure shows the K_S- and I-band light curves dominated by well-defined 0.4–0.5 and 1.5–2 mag dips, respectively. Their minima (indicated by marks) occurred at $JD - 2450000 \approx 6505$, 6851 ($K_S$), 7848 ($I$), and 8250 ($K_S$)—the exact moments are impossible to estimate due to non-uniform sampling and asymmetric properties of the dips. The total duration time of every dip is about 100 d. Assuming that all the four dips were produced by the same obscuring body, e.g. a single disc warp or a dusty cloud, a simple consideration suggests that perhaps for some not yet understood reason the dips occur in 350–400 d pairs roughly every 1340–1400 d.

Although the K_S- and I-band observations were obtained during different epochs, similar depth of all three dips observed in the K_S band suggests that it was also the same during the OGLE run. If it is the case, then the stronger light lost in the I band could suggests occultation of a several thousand Kelvin hot source, most likely the central star and/or the very inner (within 0.1 au) disc. This suggests large (60–80 deg) inclination i of the disc. Typical inclination found for AA Tau-types stars by McGinnis et al. (2015) is about 70 deg and we will assume this value for the disc inclination of Gaia21bty throughout this paper.

4.2 Light variations during and after the outburst

Based on Fig. 1a, the sudden brightness increase from the quiescent phase ($G \approx 20.1$ mag in the second half of 2020) to the maximum ($G = 17.28$ mag) lasted no longer than 4 months. Assuming the typical quiescent (but also 'uneclipsed') state at $G = 20.2$ mag, the total brightening in the G band would be $\Delta G = 2.9$ mag. Accordingly, by comparison of the VVV/VVVX data obtained out of dips during 2018 August, and the *NTT*/SOFI data taken on 2021 May 6, we estimate brightening of $\Delta J = 2.14$, $\Delta H = 2.06$, and $\Delta K_S = 2.24$ mag. Our ΔK_S is similar as observed in spectroscopically confirmed eruptive stars by Contreras Peña et al. (2017b). Comparison of the NEOWISE data gathered in fall 2018 and in spring 2021 results in $\Delta W1 = 1.72$ and $\Delta W2 = 1.61$ mag.

In contrast to Gaia17bpi (Hillenbrand et al. 2018) and Gaia18dvy (Szegedi-Elek et al. 2020), it is not clear whether the gradual brightness rise in $W1$ and $W2$ bands starting (perhaps) in the second half of 2019 or at the beginning of 2020 (i.e. about 0.75 yr earlier than in the optical *Gaia* light curve) is significant, or is a typical stochastic variation within the quiescent state. If it is really caused by the *outside-in* mechanism considered by the authors for the two aforementioned FUors, then assuming 0.2–1 $M_\odot$ for the stellar mass of Gaia21bty, and that the outburst propagated inward in the disc dynamical time-scale (i.e. comparable to the Keplerian period at the disturbed disc annuli), the time difference of 0.75 yr suggests that the outburst could have started at 0.5–0.8 au.

After the maximum around 2021 February–April, Gaia21bty started to fade. Interestingly, the fading process is not occurring monotonically: Based on the *Danish* telescope and *Gaia* spacecraft

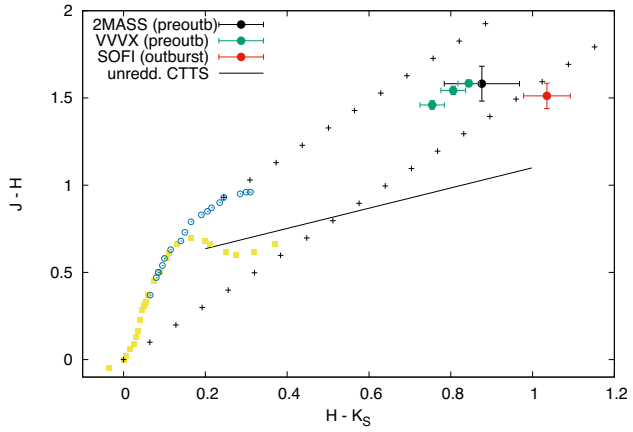

Figure 7. $J-H$ versus $H-K_S$ colour–colour diagram prepared from pre-outburst (2MASS and VVVX) and outburst (SOFI) data of Gaia21bty. The squares represent the zero-age main-sequence stars, while the open circles represent the giant branch (Bessell & Brett 1988). The black line is the locus of unreddened CTTS (Meyer, Calvet & Hillenbrand 1997). The two parallel lines formed from pluses represent the reddening path; the step represents the reddening by additional 1 mag in A_V.

data, in 2022 April, i.e. about a year after the maximum, when the star almost reached the pre-outburst level ($G = 19.93$ mag), we observed brightening that reached $\Delta V = 1.3$ mag. A second brightening was observed in October: The *Gaia* spacecraft data obtained on 2022 October 3 showed the star at $G = 20.37$ mag (typical for the pre-outburst stage), while those obtained barely 18 d later (2022 October 22) showed the star brighter by 1.28 mag. The $V = 21.78$ mag measured by the *Danish* telescope 1 d earlier is even higher than during the April 2022 brightening. The 2023 data, obtained in February–April, show continuation of this variability pattern.

Different behaviour is observed by NEOWISE. After a little brightness drop in $W1$ and $W2$ bands in 2021 August 24, which occurred a few months after the maximum, in 2022 the brightness of Gaia21bty increased a bit and roughly stabilized. We emphasize that the first NEOWISE epoch (March 13) was collected simultaneously with our *Danish* telescope observations, which clearly shows that the optical brightness reached a minimum in 2022 ($V = 23.48$ mag). This means that the post-outburst IR emission is not as strongly correlated with the optical one, as during the first outburst stage. Specifically, the IR emission has remained strong, while the optical flux has dropped but varied.

In spite of the poor photometric sampling, it appears that the optical $\sim$1 mag brightenings superimposed on the gradual fading are occurring with about a few weeks frequency. They may look like short accretion bursts at first glance, what would mean that the inner disc has not yet returned to the equilibrium. However, a competing explanation by extinction variations will be discussed in Section 4.3.

4.3 Colour–magnitude and colour–colour diagrams: determination of A_V during the quiescent phase

Analysis of the colour variations of Gaia21bty before and during the outburst is not possible in optical bands because no simultaneous multifilter data are available. Therefore such analysis for the *pre-outburst-to-maximum* stage is only possible for the JHK_S and (NEO)WISE data. Accordingly, the VR_CI_C and NEOWISE data enable similar analysis for the *maximum-to-quiescence* stage.

Pre-outburst-to-maximum: In Fig. 7 we present the $J-H$ versus $H-K_S$ colour–colour diagram and the empirical position of unreddened CTTS established by Meyer et al. (1997). Both the pre-outburst and the outburst colour indices of Gaia21bty indicate strong reddening, as previously inferred from the optical photometry. The analysis made in the previous section indicates that it could be Class II rather than Class I (or flat spectrum) object, therefore this diagram can be used to estimate the interstellar visual extinction A_V during quiescence. Assuming $R_V = 3.1$ for Cardelli, Clayton & Mathis (1989) extinction law, we obtained $A_V = 8.0 \pm 0.5$ mag during the brightest epoch covered with IR pre-outburst observations (Fig. 7). Values larger by 1.2–1.3 mag (up to $A_V = 9.3$ mag) are derived for epochs representing fainter stages, i.e. the local dip events, as obtained from the 2MASS and the reddest VVV/VVVX data points. Note that the arrangement of the VVV/VVVX colour indices exactly along the extinction vector is in line with the dipper classification (Section 4.1). We will use other methods for A_V determination in the outburst stage in Sections 4.4 and 4.6.

Near-IR colour–magnitude diagrams, IR colour index versus time, and colour–magnitude diagram based on NEOWISE photometry are shown in Figs 8a, b, c, and d, respectively. According to the colour–magnitude diagrams composed of the ground-based JHK_S data obtained simultaneously during five nights (Figs 8a and b), the variability visible during the pre-outburst stage can also be explained by the A_V increase by 1.2–1.3 mag (indicated by the half-arrow in the figure). We note that during the outburst, the *NTT*/SOFI marked by red, and the NEOWISE data points marked by grey-through-yellow (to indicate the point from 2020—the very beginning of the outburst), - to red (to indicate the point from 2022 March 13—the maximum itself), do not vary along the extinction path (Figs 8a, b, and d). Also, the $W1-W2$ colour index appears to be stable within the error bars prior and during the outburst maximum, although not in the post-outburst phase Fig. 8c).

Maximum-to-quiescence: Based on the diagrams composed of the NEOWISE (Fig. 8d), the *NTT*/EFOSC2 and the *Danish*/DFOSC VR_CI_C data (Figs 8e and f), the brightness evolution from the maximum to the quiescence appears to vary along the extinction path. We note, however, that these optical bands probe similar spectral regions, which makes it difficult to differentiate from changes caused by variable accretion (see e.g. in figure 7 in Szabó et al. 2021).

Interestingly, whereas the *Danish*/DFOSC data closely follow the extinction vector calculated for $R_V = 3.1$, the R_C-I_C colour index observed at the SAAO in 2021 August–October, i.e. just after the maximum, is redder by 1 mag at the same R_C brightness (Fig. 8f). Publicly available technical documentation of these instruments shows that the large deviation cannot be caused by very different filter and/or CCD chip sensitivity curves. Also the SAAO data were reduced in two independent ways and the results are the same within the measurement errors. This apparently real discrepancy could be explained by the assumption that the FUor outburst continues, but the post-maximum light drop and erratic variations are caused by matter composed of different grain sizes, characterized by different *total-to-selective* extinction ratios. If it is the case, then $R_V = 0.6$–1 would be required to explain the changes between these SAAO points and the brightest points obtained by the *NTT* ($R_C = 19.00$ mag) and the *Danish* telescope ($R_C = 19.48$ mag).

This view seems to be supported by 2022 NEOWISE data. They show that the $W1$ and $W2$ magnitudes measured after the maximum (which is indicated by the red point) also faded along the extinction path (i.e. the red, orange, pink, and blue points in Fig. 8d).

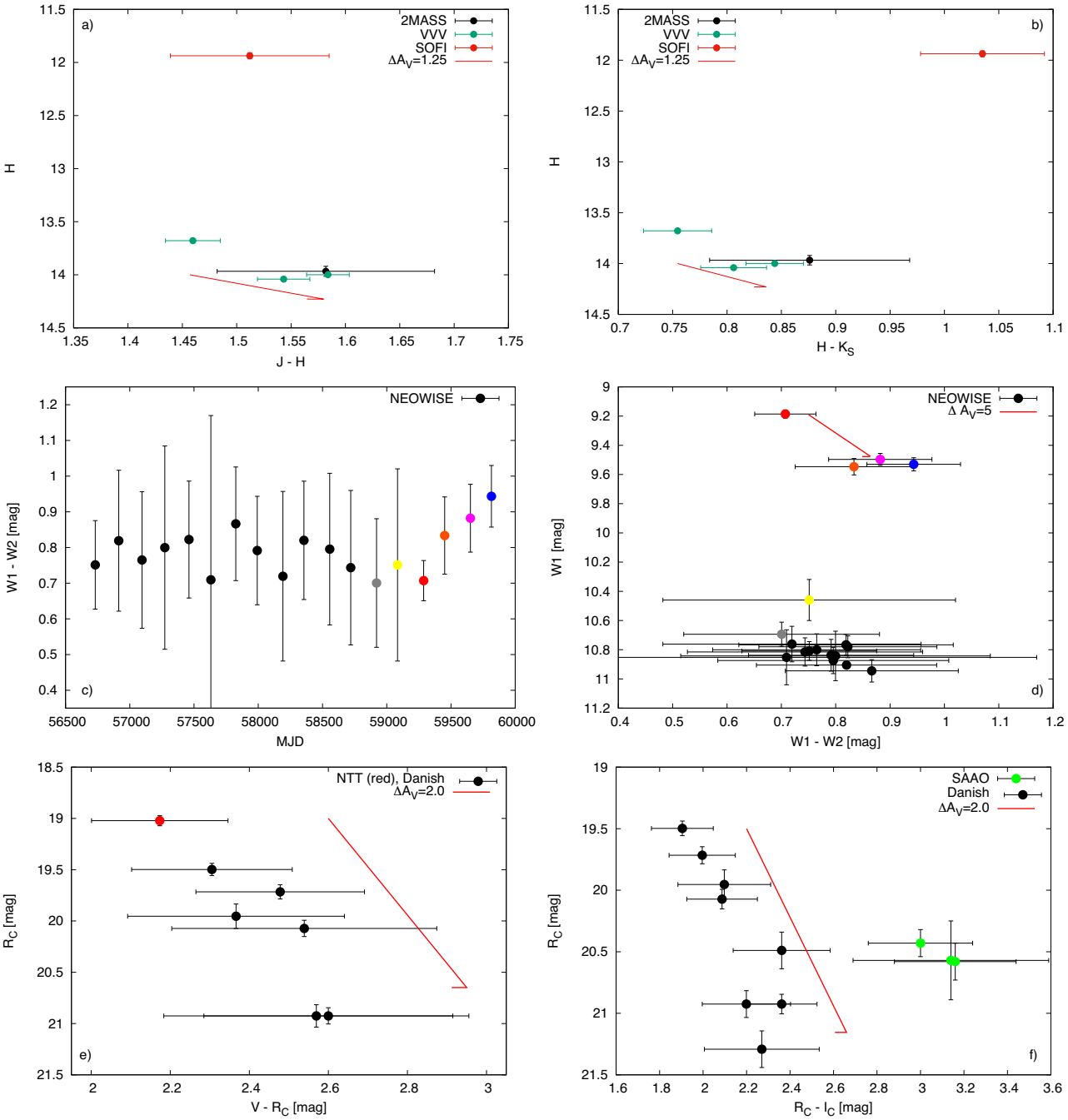

Figure 8. Colour–magnitude diagrams from JHK_S pre-outburst (2MASS, VVV, and VVVX) and outburst (SOFI) data of Gaia21bty (panels a and b). Panel c shows $W1-W2$ colour index in function of time, while panel d shows colour–magnitude diagram for pre and outburst phases based on NEOWISE $W1$ and $W2$ data. The outburst points in panels (c) and (d) are coloured in the same way to facilitate navigation. The last two panels (e and f) show the $V-R_C$ and R_C-I_C versus R_C diagrams, constructed from the data obtained in three observatories in the maximum and during the oscillations occurring during the gradual brightness decrease. Red half-arrows indicate reddening vectors for $R_V = 3.1$ and given A_V increase, as indicated in the legends.

$\Delta A_V = 5$ mag is required to explain the drop observed in the IR bands. Interestingly, during the lowest brightness noticed in post-maximum NEOWISE data on 2021 August 24, the nearly simultaneous SAAO observations suggested low R_V, as discussed above. If these variations are caused by a dusty cloud, its maximal diameter would be of 2 au to produce the observed effect in NEOWISE bands (assuming the maximum inner disc temperature of 6000–7000 K). Furthermore, the first 2022 NEOWISE point was obtained when the V-band brightness was also low (23.48 mag). This is an important finding, as we know that this NEOWISE measurement definitely did not coincide with one of the optical brightness peaks. All the above suggests variations caused by dust. This would be a scaled-up version of the phenomenon that occurred soon after the HBC 722 outburst and lasted longer than 1 yr (Semkov, Peneva & Ibryamov 2017). This scenario assumes a dust condensation event, caused by powerful disc wind colliding with the outer disc envelope. Such scenario was also proposed for V1057

Cyg to explain periodic dips appearing after the outburst (Szabó et al. 2021).

One can also speculate that within the framework established in Section 4.1, the post-maximum light drop could directly be linked to the dipper phenomenon observed in the pre-outburst stage. However, the current dip phenomenon would last longer than 1 yr, whereas the dips in the pre-outburst stage lasted no longer that 100 d.

Finally, as the optical and near-IR variability amplitude of Gaia21bty is relatively moderate, one cannot rule out the possibility that it shares some properties with V2492 Cyg (Aspin 2011; Covey et al. 2011; Kóspál et al. 2011; Hillenbrand et al. 2013). According to these authors, after the outburst, V2492 Cyg started to display (probably) quasi-periodic dip and rebrightening events caused by strongly variable, up to $\Delta A_V = 35$ mag, extinction. While this caused strong, typically a few magnitude variability in optical and near-IR bands, the NEOWISE mid-IR bands are relatively stable (figure 3 of Contreras Peña et al. 2023).

4.4 Determination of A_V during the outburst phase from the IR spectra

Knowing that the extinction towards FU Ori is low and relatively well determined ($A_V = 1.7 \pm 0.1$ mag; see in Zhu et al. 2007; Siwak et al. 2018b; Green et al. 2019; Lykou et al. 2022), we used another approach to determine the interstellar extinction towards our target. This method relies on a considerable similarity of all bona fide FUor spectra in *JHK* bands, and follows the idea of Connelley & Reipurth (2018) about checking how much dereddening ΔA_V should be applied to our near-IR flux-calibrated spectra to match the calibrated spectrum of FU Ori (but scaled to match the flux level of the target). Both for the *NTT*/SOFI and IRTF/SpeX spectra we obtained the best match for $\Delta A_V = 6.6$–6.7 mag. This results in $A_V = 8.35$ mag towards Gaia21bty during the outburst, and the value is consistent with that obtained in Section 4.3 during the quiescence.

4.5 Analysis of the quiescent SED: the progenitor

Using the pre-outburst data and the interstellar extinction determined in Section 4.3, we made an attempt to derive the main physical parameters of the progenitor. We assume full visibility of the star, which may in fact be not completely true given $i = 70$ deg.

In the first step, for each band we chose from the full quiescent SED (Fig. 3c) only the points that were not obtained during the dips. Then, we dereddened these selected data by means of the Cardelli et al. (1989) reddening law assuming $A_V = 8.0 \pm 0.5$ mag and $R_V = 3.1$ (Section 4.3). Subsequently, we fitted a Planck function to the near-IR (780–2200 nm) data points. We discarded the shorter wavelengths because they are certainly affected by the hot spots created during the magnetospheric accretion, while the longer by the disc radiation (Fig. 9a). As the result, we obtained effective temperature of the star of $T^{\star}_{\rm eff} = 3150^{+250}_{-100}$ K. The error bars quoted in $T^{\star}_{\rm eff}$ result from the uncertainty in A_V: $T^{\star}_{\rm eff} = 3050$ K corresponds to $A_V = 7.5$ mag, and $T^{\star}_{\rm eff} = 3400$ K to $A_V = 8.5$ mag. By integrating the respective Planck functions, we calculated three possible values of the bolometric stellar luminosity $L^{\star}_{\rm b}$ at $1.98^{+0.37}_{-0.36}$ $L_{\odot}$ for 1.3 kpc, $3.38^{+0.63}_{-0.61}$ $L_{\odot}$ for 1.7 kpc, and $7.31^{+1.37}_{-1.32}$ $L_{\odot}$ for 2.5 kpc. During the Planck fitting to the data dereddened by $A_V = 8.0$ mag, we also established preliminary value of the stellar radius $R^{\star}$ at about 4.5, 6, and 8.5 $R_{\odot}$ for $d = 1.3$, 1.7, and 2.5 kpc, respectively.

We also estimated the stellar luminosity and the radius following the procedure described in full in Fiorellino et al. (2021) and applied in section 4.3.2 of Cruz-Sáenz de Miera et al. (2022). Assuming

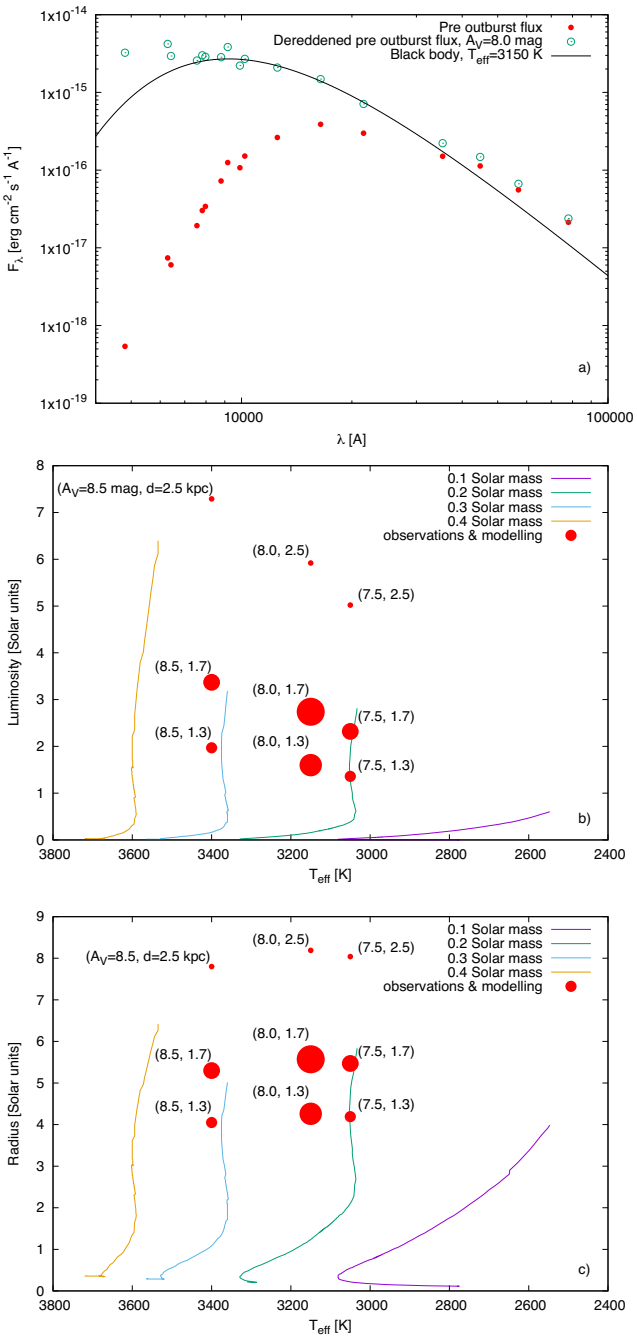

Figure 9. Results of pre-outburst data modelling (a). Position of the star in the H–R diagram based on modelling results (Pecaut & Mamajek 2013) and calibration (panels b and c); those obtained with the assumption of the most optimal set of parameters ($A_V = 8.0$ mag and d = 1.3 and 1.7 kpc) are indicated by the largest dots.

that Gaia21bty shares properties common with Class II objects, we made use of the Pecaut & Mamajek (2013) *spectral type–effective temperature* empirical relation presented in table 6 of their paper. According to this relation, the most likely spectral type is M4, but given the uncertainty in the effective temperature the full possible spread is M2–M5. Then, using $m_J = 15.138(7)$ corrected for the appropriate value of reddening (i.e. brightened by 2.109 mag for A_V =7.5 mag, 2.249 mag for 8.0 mag, and 2.390 mag for 8.5 mag), and bolometric corrections presented by the above authors for respective

Table 3. Physical parameters of the progenitor, as obtained in Section 4.5. Those marked by bold represent the most likely set.

d (kpc)	A_V (mag)	$T_{\rm eff}^{\star}$ (K)	$M_{\rm b}^{\star}$ (mag)	$L_{\rm b}^{\star}$ ($L_\odot$)	$R^{\star}$ ($R_\odot$)
1.3	7.5	3050	4.41	1.36	4.19
	8.0	3150	4.23	1.60	4.26
	8.5	3400	4.00	1.97	4.05
1.7	7.5	3050	3.83	2.32	5.47
	8.0	**3150**	**3.65**	**2.74**	**5.57**
	8.5	3400	3.42	3.37	5.30
2.5	7.5	3050	2.99	5.02	8.04
	8.0	3150	2.81	5.92	8.19
	8.5	3400	2.58	7.29	7.80

Table 4. Physical parameters of the disc during the outburst maximum. Those marked by bold represent the most likely set. Outer disc radius was set to 0.6 au and inclination to 70 deg during all computations.

$R_{\rm in}$ ($R_\odot$)	d (kpc)	$L_{\rm b}^{d}$ ($L_\odot$)	$M\dot{M}$ ($M_\odot^2$ yr^{-1})	A_V (mag)
2.0	1.3	20.2	2.7×10^{-6}	7.70
	1.7	**43.0**	$\mathbf{5.7 \times 10^{-6}}$	**8.20**
	2.5	135.1	1.8×10^{-5}	8.80
4.2	1.3	10.7	3.1×10^{-6}	5.40
5.6	1.7	17.8	7.2×10^{-6}	5.35

effective temperatures, we calculated the bolometric magnitude $M_{\rm b}^{\star}$ of our target for three values of the distance (1.3, 1.7, and 2.5 kpc), and then the respective luminosities ($L_{\rm b}^{\star}$) are $1.60^{+0.38}_{-0.24}$ $L_\odot$, $2.74^{+0.63}_{-0.43}$ $L_\odot$, and $5.92^{+1.39}_{-0.91}$ $L_\odot$. The respective stellar radii calculated with the assumption that the star radiates like a blackbody are 4.26, 5.57, and 8.19 $R_\odot$. These values are similar, although systematically slightly smaller than obtained from the Planck distribution fitting, which may result from the fact that the accretion luminosity, unaccounted by the first method, is now roughly subtracted. We list the results in Table 3.

Knowing the effective temperature and luminosity, we used the evolutionary tracks for solar composition calculated by Siess, Dufour & Forestini (2000) to determine a stellar mass of $0.23^{+0.08}_{-0.03}$ $M_\odot$. Based on the same tracks, we determined a formal age of 3600–3700 yr only, and (independently of the previous methods) a stellar radius of 4.65–5.75 $R_\odot$, which is similar to the one obtained using the Pecaut & Mamajek (2013) calibration. We plot the evolutionary tracks and stellar parameters obtained by means of the Pecaut & Mamajek (2013) relation in Figs 9b and c. According to the evolutionary tracks, distance higher than 2 kpc seems to be unlikely, as it leads to the large stellar radius that is very atypical for young low-mass stars.

Our results suggest that Gaia21bty could be a very young, rapidly contracting star. Long-term spectrophotometric monitoring in the quiescent state is necessary to check the real influence of the accretion on the blue and longer parts of the spectrum, in order to let us determine the effective temperature and the radius of the star with a better confidence.

4.6 Analysis of the outburst SED

To study the outburst physics of Gaia21bty in detail, we used the disc model introduced by Kóspál et al. (2016) for HBC 722, and then applied to other FUors (for a summary see e.g. Szabó et al. 2021, 2022). We fitted the outburst SED constructed from photometric data obtained close in time to the brightness peak, in 2021 May (see Fig. 3c). First, the errors of all data points in this SED were conservatively assumed to be 5 per cent. Then, based on the dipper nature of Gaia21bty, we set the disc inclination to $i = 70$ deg. The distance was set to $d = 1.7^{+0.8}_{-0.4}$ kpc, while the inner disc radius to $R_{\rm in} = 2$ $R_\odot$, like for FU Ori in Zhu et al. (2007).

Our best-fitting model resulted in an outer disc radius 0.6 au (note that this is similar to the value estimated by our simple thought experiment in Section 4.2), disc bolometric luminosity $L_{\rm b}^{d} = 43.0^{+92.1}_{-22.8}$ $L_\odot$, $M\dot{M} = 5.7^{+12.3}_{-3.0} \times 10^{-6}$ $M_\odot^2$ yr^{-1}, and $A_V = 8.2^{+0.6}_{-0.5}$ mag. For clarity but especially to show how the results depend on the assumed distance, we list these values also in Table 4. The large uncertainty in $L_{\rm b}^{d}$ and $M\dot{M}$ is caused by uncertainty about the distance. Taking $d = 1.7$ kpc, and the stellar mass $0.23^{+0.08}_{-0.03}$ $M_\odot$, the mass accretion rate $\dot{M} = 2.5^{-0.6}_{+0.4} \times 10^{-5}$ $M_\odot$ yr^{-1}. Based on results listed in Table 4, larger $\dot{M}$ can be derived for $d = 2.5$ kpc, and smaller for 1.3 kpc.

We also explored models with larger inner disc radii, e.g. equal to the stellar radius obtained in Section 4.5. As $d = 2.5$ kpc lead to stellar parameters inconsistent with our current knowledge on the early stellar evolution, we considered only those obtained for $d = 1.7$ kpc ($R_{\rm in} = 5.6$ $R_\odot$) and for $d = 1.3$ kpc ($R_{\rm in} = 4.2$ $R_\odot$), in which the stellar radii were inferred from the Pecaut & Mamajek (2013) calibration. Although the fit quality (as measured by χ^2) was now twice better than for the model with $R_{\rm in} = 2$ $R_\odot$, they resulted in $A_V = 5.4$ mag, $M\dot{M} = 3.1 \times 10^{-6}$ $M_\odot^2$ yr^{-1}, $L_{\rm b}^{d}$=10.7 $L_\odot$, and $A_V = 5.35$ mag, $M\dot{M} = 7.2 \times 10^{-6}$ $M_\odot^2$ yr^{-1}, $L_{\rm b}^{d}$=17.8 $L_\odot$, respectively (Table 4). These last two A_V values are, however, significantly lower than the A_V values estimated from the outburst spectra (8.35 mag, Section 4.4), or from the colour–colour diagram in the quiescence (8 ± 0.5 mag, Section 4.3). Based on these, we accepted $R_{\rm in} = 2$ $R_\odot$ for the 2021 May outburst SED. Although this is in obvious conflict with the stellar radii determined in the previous section, we cannot exclude the scenario, in which due to the enhanced accretion the inner disc matter (a boundary layer) wrapped on to the intermediate latitudes of the star. Other possibility assumes that the disc merges with the bloated star without boundary layer formation, as considered by Milliner et al. (2019).

We also constructed a SED from data points obtained 1 yr later, in 2022 March 13. In the lack of near-IR observations, we built this SED from ground-based optical photometry and NEOWISE data. Interestingly, this more recent SED exhibits a shape very different from the one obtained at peak brightness: While in the optical the source dropped significantly since 2021 May, the mid-IR flux levels remained approximately constant. In order to check whether our simple accretion disc model could reproduce this colour change, we run our best model for $d = 1.7$ kpc on the 2022 March SED, fixing the disc geometry parameters. The data points can be well fitted with our disc model, with a luminosity $L_{\rm b}^{d} = 38.0$ $L_\odot$, $M\dot{M} = 5.1 \times 10^{-6}$ $M_\odot^2$ yr^{-1}, and $A_V = 10.30$ mag. These results suggest that while the accretion rate slightly decreased after the outburst peak, the main factor behind the detected brightness changes was a sudden rise of the extinction by about 2 mag, which explains also the unexpected colour changes.

A rise of extinction is a physically plausible explanation during an outburst, since the accretion process can rearrange the structure of the inner disc (e.g. Mosoni et al. 2013). To explore this possibility, we fitted the 2022 March SED by fixing A_V to 8.20 mag, the value we obtained for the outburst peak epoch in 2021 May, and let $R_{\rm in}$ to vary. We could achieve a fit of similarly quality than before, obtaining the following parameters: $L_{\rm b}^{d} = 18.4$ $L_\odot$ and $M\dot{M} = 5.7 \times 10^{-6}$ $M_\odot^2$ yr^{-1}. Based on these results, it is possible to interpret the brightness evolution of Gaia21bty between 2021 May and 2022 March by keeping the accretion rate and the extinction unchanged, but increasing $R_{\rm in}$ from 2.0 to 4.45 $R_\odot$. Physically, this increase

in $R_{\rm in}$ might mark a depletion of the innermost part of the disc as the piled-up material falls onto the star during the outburst, converting the inner disc optically thin. While it is a reasonable alternative scenario in addition to our previous models where A_V changed, it is also possible that we observe the outcome of a simultaneously increasing A_V and a growing $R_{\rm in}$ in the Gaia21bty system.

Our modelling of the SED in 2022 March, either the fixed $R_{\rm in}$ or the fixed A_V scenarios, implies that the extinction remained relatively high, larger, or equal to 8.2 mag. We can confirm this conclusion with observations. If the extinction was significantly lower, we probably would be able to detect our target in the *B*-band images taken in the maximum by *NTT*/EFOSC2 and by *Danish*/DFOSC during the brightening on 2022 April 12. This is obtained as follows: Gaia21bty is detected with $S/N = 7$–8 on each single 300 s *V*-band images obtained on 2022 April 12, so that a 50 s exposure would suffice to detect the star with $S/N = 3$. According to Pecaut & Mamajek (2013) for Class II star of M4 spectral type the intrinsic $(B - V)_0 = 1.53$ mag. The reddening ($R_V = 3.1$ and $A_V = 5.4$ mag) would lead to $E(B - V) = 1.76$ mag (versus 2.61 mag for $A_V = 8$ mag), so Gaia21bty would be 3.29 mag fainter in *B* than in *V*. So in order to reach $S/N = 3$ in the *B* band, we would need to integrate for about 1040 s. However, the total integration time in the *B* band was 1500 s. Thus, the non-detection supports A_V larger than 6.7 mag.

4.7 Analysis of the outburst spectral properties

In spite of the mass accretion rate typical for FUors, the short maximum duration of the outburst in optical light indicates that Gaia21bty may not be a bona fide FUor. However, our spectra are dominated by features seen typically only in FUors, as described below.

4.7.1 Comments on individual lines

In Fig. 10, we show optical and near-IR spectra normalized to unity at the continuum level. The major spectral lines we detected are indicated by vertical dashed lines.

The optical Keck II/ESI spectrum obtained at the maximum light shows a weak absorption signature of Li I (6707.76, 6707.97 Å). It is barely detectable in the original spectrum due to the low *S/N*, but the visibility can be improved by 3-pixel Gaussian smoothing. The manually measured radial velocity (RV) at 2/3 depth of the smoothed line is about -36 ± 2 km s^{-1} (Fig. 11a). Sharp and deep K I doublet (7664.90 and 7698.96 Å) and the O I 7774 Å triplet absorptions are also present, and these lines are centred at the same velocity (-35 ± 1 km s^{-1}) as lithium. This agreement gives hint that this value can be considered as the systemic RV of Gaia21bty with respect to us (see also Section 4.7.2).

The IR *J*-band spectra obtained in the maximum by *NTT*/SOFI, and a second obtained during the brightness decrease by IRTF/SpeX, show metallic absorption lines like Al I at 1.312 and 1.315 μm, and water vapour bands in absorption starting with a sharp drop at 1.33 μm and leading to the characteristic triangular shape of the *H*-band spectra. The *H*-band spectra appear to be dominated by the Brackett series in absorption—those visible in one spectrum only, or with uncertain detection in both spectra, are labelled with a question mark in Fig. 10. Metals are also present in absorption, such as FeI and Mg I, one of them (at 1.588 μm) blending with Br 14-4 and SiI. Both *K*-band spectra show the CO bands in strong absorption. Due to the time span of 48 d we compared these spectra to check for difference in CO bands absorption depth, following Szabó et al. (2021), but we did not notice any significant changes. The IRTF/SpeX spectrum also reveals Na 2.208 μm in absorption; however, no firm indications of Ca 2.256 μm are present. There is no consensus about the (non)detection of Brγ in both spectra. All these spectral features listed so far are common for FUors.

P-Cygni profiles typical for FUors and indicative of outflow from a disc wind, are seen in all three Ca II IRT lines (8498.02, 8542.09, and 8662.14 Å; Fig. 11b). NaD (5889.95 and 5895.924 Å) seem to exhibit P-Cygni profile as well, but the *S/N* in this region is too small (about 2) to claim this with full certainty. We also probably detect Na I line in both *J*-band spectra, and the line also exhibits P-Cygni profile. The K I doublet and O I triplet mentioned above have extended blueshifted absorption components to their profiles, though no emission component.

The most prominent spectral lines seen in emission are Hα (6562.82 Å) and He I 1.083 μm, along with weak Paβ (12821.6 Å). We also see the IR O II line in emission, but only in the spectrum taken in the fading.

The Hα profile is double-peaked with a blueshifted absorption component, most likely due to the superposition of emission and an absorbing wind component (Fig. 11c). The emission components peaks around -170 and $+33$ km s^{-1}, and the absorption has a minimum at about -55 km s^{-1}. The line peaked 6.5× times over the continuum level which is significantly more than observed (∼1.1–1.4) in a few FUors, namely HBC 722, V960 Mon, Gaia17bpi, and Gaia18dvy during their first outburst phases (Semkov et al. 2010; Miller et al. 2011; Kóspál et al. 2016; Hillenbrand et al. 2018; Park et al. 2020; Szegedi-Elek et al. 2020). In addition, the Hα line in Gaia21bty did not evolve to a pure P-Cygni profile like in the above FUors, the same as it was seen in the spectra taken in the early outburst stages of HBC 722 (Semkov et al. 2010; Kóspál et al. 2016). We speculate that (at least) during the time when our optical spectrum was taken, the accretion rate was still insufficient to drive a disc wind massive enough to develop an even deeper absorption component, capable of producing typical P-Cygni profile, like in the Ca II triplet (Fig. 11b). This is supported by a comparison of HBC 722 and Gaia17bpi spectra obtained at similar outburst stages, which reveals that the P-Cygni profile in the Hα line appeared later in HBC 722 than in Gaia17bpi (Hillenbrand et al. 2018). Similar evolution of Hα line profile was presented by Park et al. (2020), who reported that in parallel with the brightness decrease of V960 Mon, the profile evolved from a pure P-Cygni shape to being dominated by an emission component. We also note that the Hα line in Gaia21bty has a strength similar to that observed during the maxima of V899 Mon, which is known to be an 'intermediate' eruptive star between FUors and EXors (Ninan et al. 2015; Park et al. 2021). Continued monitoring should reveal temporal changes occurring on a longer time-scale and their possible correlations with the accretion rate in Gaia21bty.

The resolution of our *J*-band spectra is insufficient to study the He I 1.083 μm line shape in detail, but it appears to be fairly symmetric and shows only the emission component. According to figure 4 in Erkal et al. (2022) who studied the line shape in 117 Class II sources having disc inclinations determined by ALMA, this profile shape is common for stars observed at high inclinations, which is in line with the dipper nature of Gaia21bty. The authors also mentioned that sources showing only emission component tend to be associated with known jets and outflows, and that they are more common for younger stars. Thus the fact that we still see the He I 1.083 μm line in emission, can indicate a powerful outflow, perhaps collimated into a jet. No more outflow or jet indicators are observed in Gaia21bty, but

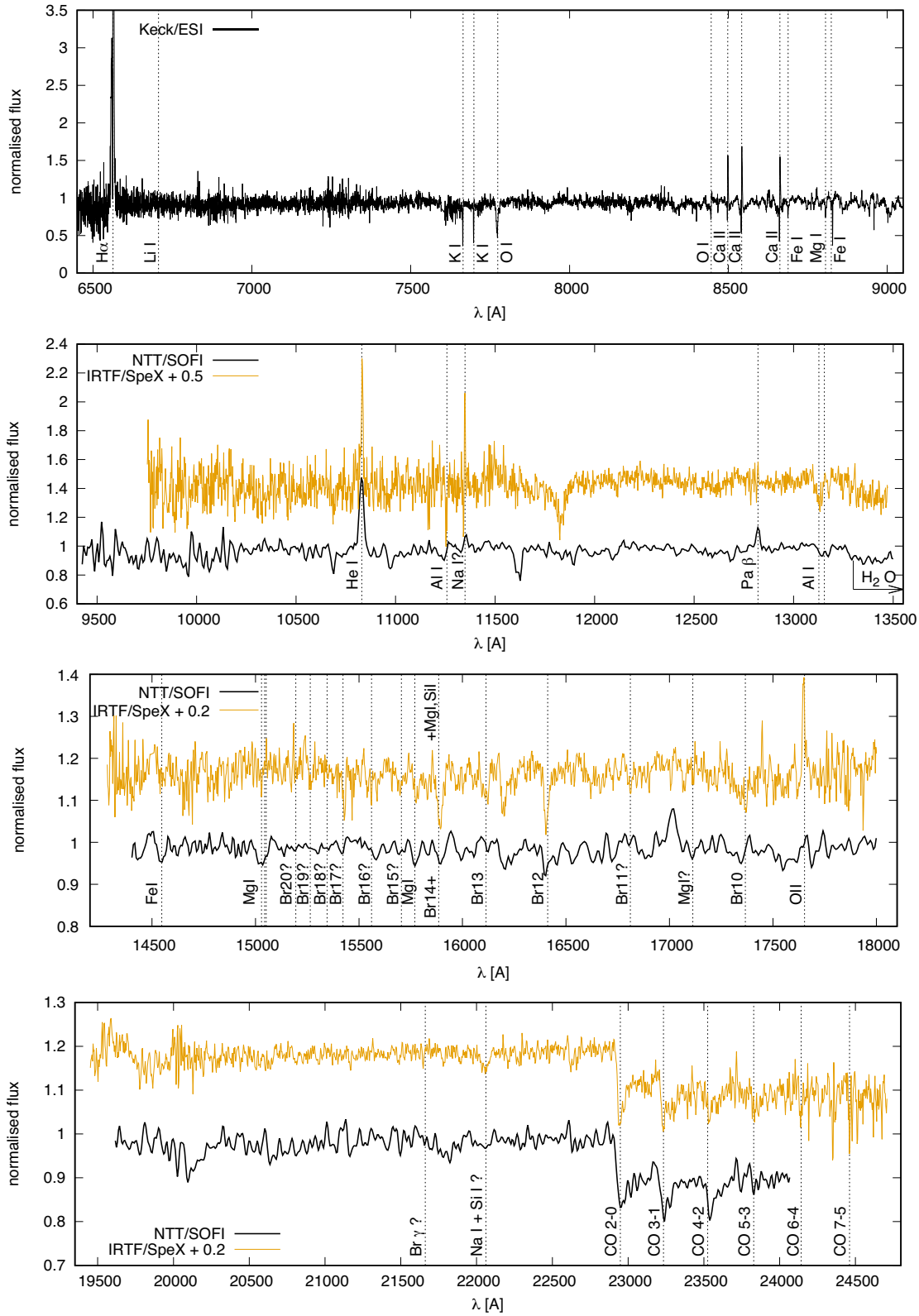

Figure 10. Optical Keck/ESI, and near-IR *NTT*/SOFI and IRTF/SpeX spectra (shifted by 0.5 or 0.2 for clarity), with major detected spectral lines marked with dotted vertical lines. Hα peaks at a normalized flux of 6.5 (so it is cut off here), while the spectral region before this line is dominated by noise.

this is not unexpected given the *S*/*N* of our spectra shortward of 6500 Å, and the fact that the spectrograph slit was randomly positioned with respect to the putative jet vector.

We also observed Paβ in emission in the *NTT*/SOFI spectrum obtained at the maximum light, but not in the IRTF/SpeX spectrum obtained 48 d later. Taking advantage that the line belongs to the

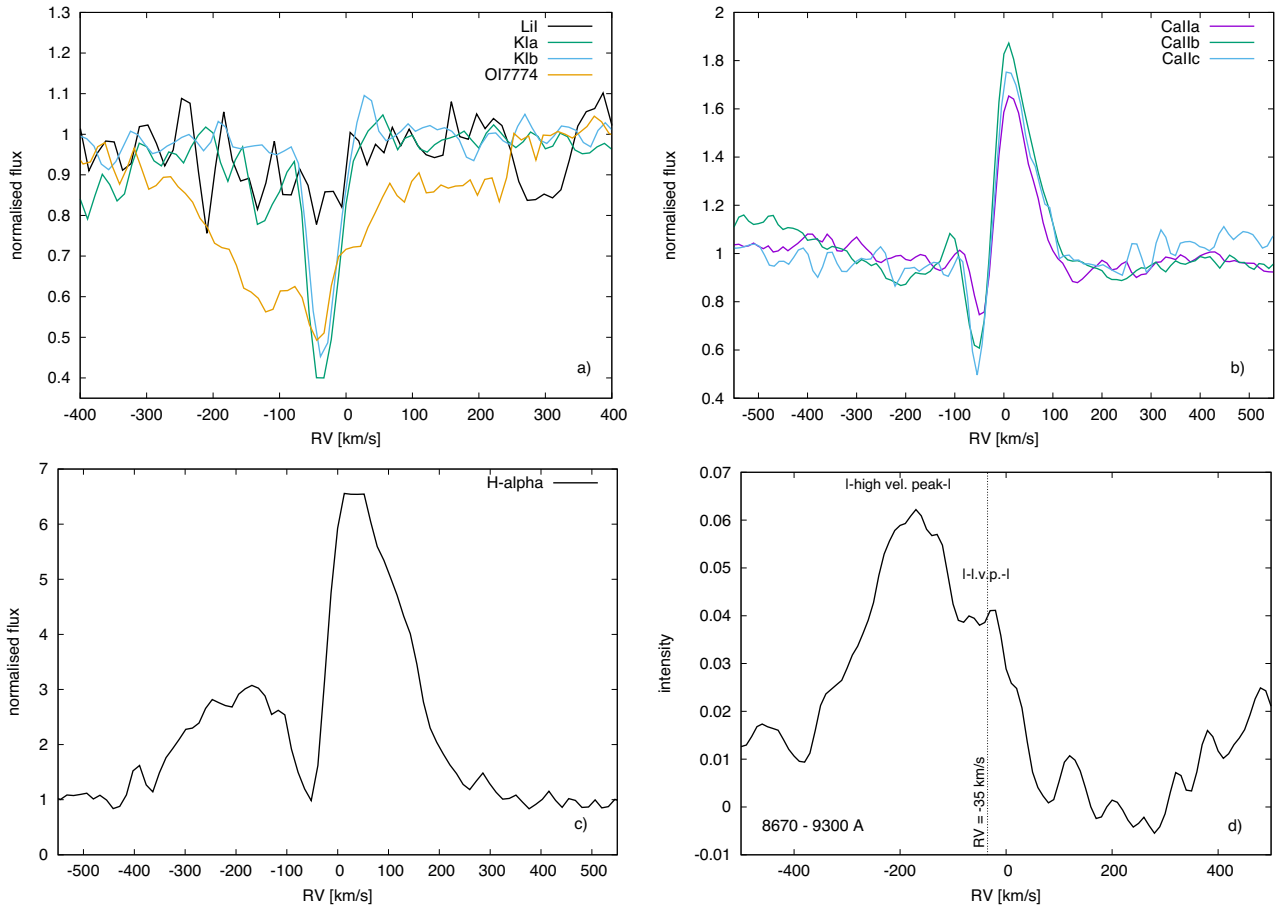

Figure 11. Detailed look onto a few lines observed by Keck/ESI in the maximum. The last panel shows broadening functions (BF) calculated for the 8670–9300 Å spectral region. Preliminary systemic RV, determined by means of the three sharp metallic lines shown in panel a, is also indicated.

well-known accretion tracers in Class II stars, we measured the line flux $F_{\mathrm{Pa}\beta}$ to independently estimate the mass accretion rate. We decided to perform this check in spite of the fact that Gaia21bty is undergoing enhanced accretion and having properties more typical for FUors. First, the original flux-calibrated spectra were corrected for the interstellar extinction assuming $A_V = 8.35$ mag. Then, following the recipe from section 3.2.5 in Park et al. (2021), the line flux was measured 100 times with random Gaussian errors multiplied by the observation errors. The standard deviation derived from the all measurements was adopted as the uncertainty of the line flux. As the result we obtained $F_{\mathrm{Pa}\beta} = 4.82 \pm 0.06 \times 10^{-14}$ erg s^{-1} cm^{-2}. Then, following equations number 1–3 in their paper and using the respective coefficients from Alcalá et al. (2017), for $d = 1.7$ kpc, stellar radius of 5.6 R$_\odot$ and the stellar mass of 0.23 M$_\odot$, we obtained $\dot{M} = 3.1 \times 10^{-7}$ M$_\odot$ yr^{-1}, i.e. 2 orders of magnitude less than from the disc modelling. This is giving hint that accretion at the maximum brightness of Gaia21bty was no longer magnetospherically controlled, as it would be if Gaia21bty were an ordinary EXor.

4.7.2 BF analysis of the Keck/ESI absorption spectrum

The better-exposed 8600–10300 Å spectral range shows numerous broad absorption lines, at first sight formed in the disc atmosphere, which could be used to refine the RV of Gaia21bty relative to us. However, the initial RV analysis of a few randomly chosen single lines indicated about three times higher broadening than observed in other classical (Hartmann & Kenyon 1985; Kenyon & Hartmann 1989) and most recent FUors (Park et al. 2020). This is actually not an unexpected effect, as Gaia21bty is an embedded object and its radiation is severely modified by the disc wind. Nevertheless, we decided to amplify the disc component by means of the BF method (Rucinski 2012 and references therein). The method determines the Doppler broadening kernel in the convolution equation transforming a sharp-line spectral template into the observed spectrum using information carried by all absorption lines from the investigated region. This technique was successfully applied for analysis of RVs and surface mapping in contact and close binary stars, two CTTS RU Lup and IM Lup (Siwak et al. 2016), and also the FUor star V646 Pup. In the latter case Siwak, Ogłoza & Krzesiński (2020) obtained well-defined BFs fairly stable over many years, dominated by the disc profile and showing only a slight signature of the high velocity disc wind outflow in the absorption spectrum. However, the case of Gaia21bty is very different.

We analysed the 8670–9300 Å region using a dozen of synthetic stellar templates. The template spectra were prepared using the PHOENIX data base (Husser et al. 2013), they have $T_{\mathrm{eff}} =$ 4500–6500 K with 500 K increment, and $\log g = 0.0$–2.0 with 0.5 increment. We obtained the best defined BF profiles with the templates having $T_{\mathrm{eff}} = 5500$ K and $\log g = 1$–1.5 (Fig. 11d). Similarly, the analysis of 9556–10256 Å region resulted in best defined BF profiles obtained with templates having $T_{\mathrm{eff}} = 4500$–

5000 K and $\log g = 0$–0.5. These values are in accordance with expectations for FUors, having a supergiant stellar spectrum with effective temperature and $\log g$ of consecutive disc annuli decreasing with the increasing distance from the star. The BF profile shown in Fig. 11d reveals that the high velocity component (marked as *high velocity peak*, peaking at about -180 km s^{-1}) dominates over the second peak, marked as *l.v.p.* (*low velocity peak*). The double-peaked BF shape carries also the information that in contrast to some specific metallic lines (see in Fig. 11a), the great majority of the absorption lines is strongly affected by the disc wind.

The high velocity peak reaching -300 km s^{-1} is formed by the disc wind, and its strength dominates absorption lines similarly like in the embedded FUor V1057 Cyg, as shown in Fig. 7 by Herbig, Petrov & Duemmler (2003), and in Fig. 10 by Szabó et al. (2021). We note that the *low velocity peak* appears to have similar mean RV as the metallic lines shown in detail in Fig. 11a. This indicates that it represents the pure, unmodified disc absorption. Due to the low brightness of Gaia21bty no high-resolution spectra can be obtained in a close future either to confirm stability of this absorption feature or to study the variation of the line broadening with wavelength, as observed in classical FUors. Unfortunately, the spectral resolution of our *JHK* spectra is 5–10× smaller than provided by ESI, which is insufficient even for rough RV measurements and line profile studies, like above.

5 CONCLUSIONS

We investigated Gaia21bty, which drew the community's attention on 2021 April 11, as a YSO showing considerable, $\Delta G = 2.9$ mag brightening, resembling those observed in other eruptive young stars. The first medium-resolution Keck/ESI visual spectrum obtained at the maximum brightness suggested that it may be a FUor (Hillenbrand 2021). We have been continuing the study by means of public-domain and our own photometric and spectroscopic data. Unexpectedly, Gaia21bty remained in the maximum only for a few months, and around 2021 May–June started to fade in the optical, though has remained bright in the mid-IR through at least late 2022.

To characterize the progenitor, we constructed the pre-outburst light curve based on images provided by sufficiently deep, public-domain surveys. The historical brightness changed very little, except for a few deep dips. The star appears to be heavily extincted ($A_V = 8$ mag), preventing significant detections shortward of the V band. At longer wavelengths, roughly beyond 8–10 μm, the source characterization is seriously limited or impossible due to the bright nebula surrounding the object. Our classification of the progenitor as a Class II disc is slightly uncertain, with a flat or even Class I-type SED not ruled out.

The luminosity of the progenitor is also uncertain, as the distance can be estimated with only a low accuracy based on the distribution of the well-determined parallaxes of other nearby YSOs and YSO-candidates. The most probable value is 1.7 kpc, but the acceptable values lie in the range 1.3–2.5 kpc. Planck function fitting to the dereddened data indicates $T_{\rm eff}^{\star} = 3150$ K and $L_{\rm b}^{\star} = 2.7$ L$_\odot$ for the star, which implies a quite large stellar radius of 5.6 R$_\odot$. According to the grid of evolutionary tracks by Siess et al. (2000) such a set of physical parameters points to a 0.23 M$_\odot$ star that has just entered the Hayashi track. These findings are challenged by our modelling of the outburst SED, as the model obtained with the stellar radius above resulted in $A_V = 5.5$ mag, which is inconsistent with that determined during the outburst based on IR spectra ($A_V = 8.35$ mag) and the fact that Gaia21bty is not detected in the B band. According to the disc model, the stellar (assumed to be equal to the inner disc) radius appears to be closer to the canonical value of 2 R$_\odot$, which assuming $d = 1.7$ kpc resulted in $A_V = 8.2$ mag, $L_{\rm b}^{d} = 43$ L$_\odot$, and $M\dot{M} = 5.7 \times 10^{-6}$ M$_\odot^2$ yr^{-1}. Assuming the stellar mass of 0.23 M$_\odot$, the mass accretion rate would be $\dot{M} \approx 2.5 \times 10^{-5}$ M$_\odot$ yr^{-1}, which is typical for FUors.

Although the light curve closely resembles those of EXors, the spectral features are typical for FUors. This includes P-Cygni profiles in (at least) the CaII triplet created by a massive disc wind. Although dominated by the emission, similar wind signature can be observed in the Hα line too. Strong blueshifted wind signatures dominate the profiles of the metallic absorption lines from the analysed 8670–10300 Å region. The IR spectra show strong CO absorption band, a series of metallic lines seen in absorption in classical FUors, and the Brγ series in absorption. Gaia21bty displays three lines with pure emission profile, namely HeI 1.083 μm, Paβ, and O II, and these lines are typically seen in CTTS and EXors, but comparison with other FUor spectra from the literature suggests that this is only because the spectra were obtained in the early stages of the outburst. Note that IR spectra obtained 48 d later show that Paβ emission most likely disappeared, while OII emission appeared or became stronger.

In conclusion, spectral features typical for classical FUors are definitely prevailing in Gaia21bty. However, the brightness started to decrease in all bands after barely 4–6 months of staying in the maximum, which is typical for EXors. As the post-outburst brightness evolution in the colour–magnitude diagrams occurs along the reddening path, and influences mostly the optical wavelengths, we cannot exclude that the outburst continues, but the inner disc and the stellar light is currently blocked. This could be due to dust condensations caused by the disc wind colliding with the outer envelope, as supported by irregular post-outburst photometric behaviour in optical bands, and fairly stable in the IR. Continued photometric and spectroscopic monitoring should let us understand better the nature of this eruption in the coming years.

ACKNOWLEDGEMENTS

This project has received funding from the European Research Council (ERC) under the European Union's Horizon 2020 research and innovation programme under grant agreement No. 716155 (SACCRED).

We acknowledge support from the ESA PRODEX Contract No. 4000132054. GM and ZN were supported by the János Bolyai Research Scholarship of the Hungarian Academy of Sciences. GM acknowledges support from the European Union's Horizon 2020 research and innovation programme under grant agreement No. 101004141.

EF acknowledges financial support from the project PRIN-INAF 2019 'Spectroscopically Tracing the Disc Dispersal Evolution (STRADE)'.

ZMS acknowledges funding from a St Leonards scholarship from the University of St Andrews. For the purpose of open access, the author has applied a Creative Commons Attribution (CC BY) licence to any Author Accepted Manuscript version arising.

This work is based in part on data obtained with the NASA Infrared Telescope Facility, which is operated by the University of Hawaii under a contract with the National Aeronautics and Space Administration.

The data presented herein were obtained at the W. M. Keck Observatory, which is operated as a scientific partnership among the California Institute of Technology, the University of California, and the National Aeronautics and Space Administration. The Observatory was made possible by the generous financial support of

the W. M. Keck Foundation. The authors wish to recognize and acknowledge the very significant cultural role and reverence that the summit of Maunakea has always had within the indigenous Hawaiian community. We are most fortunate to have the opportunity to conduct observations from this mountain.

This research is based on observations made with *ESO* telescopes at the La Silla and Paranal Observatories under programme ID: 105.203T.001. This paper is based on data obtained from the ESO Science Archive Facility.

This paper uses observations made at the South African Astronomical Observatory (SAAO).

This publication was produced within the framework of institutional support for the development of the research organization of Masaryk University.

This publication makes use of data products from the Two Micron All Sky Survey, which is a joint project of the University of Massachusetts and the Infrared Processing and Analysis Center/California Institute of Technology, funded by the National Aeronautics and Space Administration and the National Science Foundation.

This work is based in part on observations made with the *Spitzer* space telescope, which was operated by the Jet Propulsion Laboratory, California Institute of Technology under a contract with NASA.

This publication makes use of data products from the Wide-field Infrared Survey Explorer, which is a joint project of the University of California, Los Angeles, and the Jet Propulsion Laboratory/California Institute of Technology, funded by the National Aeronautics and Space Administration.

This research has made use of the NASA/IPAC Infrared Science Archive, which is funded by the National Aeronautics and Space Administration and operated by the California Institute of Technology.

This publication uses data generated via the Zooniverse.org platform, development of which is funded by generous support, including a Global Impact Award from Google, and by a grant from the Alfred P. Sloan Foundation.

We acknowledge ESA *Gaia*, DPAC, and the Photometric Science Alerts Team (http://gsaweb.ast.cam.ac.uk/alerts).

This research has made use of the Spanish Virtual Observatory (http://svo.cab.inta-csic.es) supported from Ministerio de Ciencia e Innovación through grant PID2020-112949GB-I00.

Special thanks are also due to an anonymous referee for highly useful suggestions and comments on the previous version of the paper.

DATA AVAILABILITY

Photometric data extracted from images downloaded from public archives and those obtained in this paper, are presented in the main body of the paper. Extracted spectroscopic data, our individual raw and/or calibrated images, as well as the OGLE data, can be obtained on a request to the corresponding author. All but OGLE photometric data presented in the paper but not presented in the tables were obtained from publicly available catalogues and are therefore not retyped here.

REFERENCES

Ábrahám P. et al., 2009, Nature, 459, 224
Ábrahám P. et al., 2019, ApJ, 887, 156
Acosta-Pulido J. A. et al., 2007, AJ, 133, 2020
Alcalá J. M. et al., 2017, A&A, 600, A20
Alonso-García J. et al., 2018, A&A, 619, A4
Andrews S. M., Rothberg B., Simon T., 2004, ApJ, 610, L45
Aspin C., 2011, AJ, 141, 196
Audard M. et al., 2014, in Beuther H., Klessen R. S., Dullemond C. P., Henning T., eds, Protostars and Planets VI. Univ. Arizona Press, Tucson, p. 387
Bessell M. S., Brett J. M., 1988, PASP, 100, 1134
Cardelli J. A., Clayton G. C., Mathis J. S., 1989, ApJ, 345, 245
Churchwell E. et al., 2007, ApJ, 670, 428
Cieza L. A. et al., 2016, Nature, 535, 258
Connelley M. S., Reipurth B., 2018, ApJ, 861, 145
Contreras Peña C. et al., 2017a, MNRAS, 465, 3011
Contreras Peña C. et al., 2017b, MNRAS, 465, 3039
Contreras Pena C., Naylor T., Morrell S., 2019, MNRAS, 486, 4590
Contreras Peña C. et al., 2023, MNRAS, 521, 5669
Covey K. R. et al., 2011, AJ, 141, 40
Creevey O. L. et al., 2023, A&A, 674, A26
Cruz-Sáenz de Miera F. et al., 2022, ApJ, 927, 125
Cutri R. M. et al., 2003, The IRSA 2MASS All-Sky Point Source Catalog, NASA/IPAC Infrared Science Archive, available at: http://irsa.ipac.caltech.edu/applications/Gator/
Drew J. E. et al., 2014, MNRAS, 440, 2036
Erkal J. et al., 2022, A&A, 666, A188
Fazio G. G. et al., 2004, ApJS, 154, 10
Fiorellino E. et al., 2021, A&A, 650, A43
Fiorellino E., Tychoniec Ł., Cruz-Sáenz de Miera F., Antoniucci S., Kóspál Á., Manara C. F., Nisini B., Rosotti G., 2023, ApJ, 944, 135
Fischer W. J., Hillenbrand L. A., Herczeg G. J., Johnstone D., Kóspál Á., Dunham M. M., 2023, in Shu-ichiro I., Yuri A., Takayuki M., Kengo T., Motohide T., eds, Protostars and Planets VII Vol. 534, ASP Conf. Ser., p. 355
Gaia Collaboration, 2016, A&A, 595, A1
Gaia Collaboration, 2022, A&A, 674, A1
Ghosh A. et al., 2022, ApJ, 926, 68
Green G. M., Schlafly E., Zucker C., Speagle J. S., Finkbeiner D., 2019, ApJ, 887, 93
Guo Z. et al., 2021, MNRAS, 504, 830
Hankins M. et al., 2020, Astron. Telegram, 13902, 1
Hartmann L., Kenyon S. J., 1985, ApJ, 299, 462
Henden A. A., Levine S., Terrell D., Welch D. L., 2015, American Astronomical Society Meeting Abstracts #225, p. 336.16
Herbig G. H., 1977, ApJ, 217, 693
Herbig G. H., 1989, in European Southern Observatory Conference and Workshop Proceedings. 33, Garching, Germany, p. 233–246
Herbig G. H., Petrov P. P., Duemmler R., 2003, ApJ, 595, 384
Herczeg G. J. et al., 2016, ApJ, 831, 133
Hillenbrand L. A., 2021, Astron. Telegram, 14590, 1
Hillenbrand L. A. et al., 2013, AJ, 145, 59
Hillenbrand L. A. et al., 2018, ApJ, 869, 146
Hillenbrand L. A., Reipurth B., Connelley M., Cutri R. M., Isaacson H., 2019a, AJ, 158, 240
Hillenbrand L. A. et al., 2019b, ApJ, 874, 82
Hodapp K. W. et al., 2019, AJ, 158, 241
Hodapp K. W. et al., 2020, AJ, 160, 164
Hodgkin S. T. et al., 2021, A&A, 652, A76
Holoien T. W.-S. et al., 2014, ApJ, 785, L35
Hubbard A., 2017, ApJ, 840, 6
Husser T. O., Wende-von Berg S., Dreizler S., Homeier D., Reiners A., Barman T., Hauschildt P. H., 2013, A&A, 553, A6
Kausch W. et al., 2015, A&A, 576, A78
Kenyon S. J., Hartmann L., 1989, ApJ, 342, 1134
Kochanek C. S. et al., 2017, PASP, 129, 104502
Kóspál Á. et al., 2011, A&A, 527, A133
Kóspál Á. et al., 2016, A&A, 596, A52
Kuhn M. A., de Souza R. S., Krone-Martins A., Castro-Ginard A., Ishida E. E. O., Povich M. S., Hillenbrand L. A., COIN Collaboration, 2021, ApJS, 254, 33

Kuhn M. A. et al., 2022, Astron. Telegram, 15721, 1
Lada C. J., 1987, in Peimbert M., Jugaku J., eds, Proc. IAU Symp. 115, Star Forming Regions, Cambridge University Press, Tokyo Japan, p.1
Lykou F. et al., 2022, A&A, 663, A86
McGinnis P. T. et al., 2015, A&A, 577, A11
Mainzer A. et al., 2011, ApJ, 731, 53
Marton G., Tóth L. V., Paladini R., Kun M., Zahorecz S., McGehee P., Kiss C., 2016, MNRAS, 458, 3479
Marton G. et al., 2019, MNRAS, 487, 2522
Masci F. J. et al., 2018, PASP, 131, 018003
Masci F. J. et al., 2019, PASP, 131, 018003
Meyer M. R., Calvet N., Hillenbrand L. A., 1997, AJ, 114, 288
Miller A. A. et al., 2011, ApJ, 730, 80
Miller A. A. et al., 2015, Astron. Telegram, 7428, 1
Milliner K., Matthews J. H., Long K. S., Hartmann L., 2019, MNRAS, 483, 1663
Minniti D. et al., 2010, New Astron., 15, 433
Molyarova T., Akimkin V., Semenov D., Ábrahám P., Henning T., Kóspál A., Vorobyov E., Wiebe D., 2018, ApJ, 866, 46
Moorwood A., Cuby J. G., Lidman C., 1998, The Messenger, 91, 9
Mosoni L. et al., 2013, A&A, 552, A62
Muzerolle J., Megeath S. T., Flaherty K. M., Gordon K. D., Rieke G. H., Young E. T., Lada C. J., 2005, ApJ, 620, L107
Nagy Z. et al., 2021, MNRAS, 504, 185
Nagy Z., et al., 2023, MNRAS, 524, 3344
Ninan J. P. et al., 2015, ApJ, 815, 4
Park S. et al., 2020, ApJ, 900, 36
Park S. et al., 2021, ApJ, 923, 171
Park S. et al., 2022, ApJ, 941, 165
Pecaut M. J., Mamajek E. E., 2013, ApJS, 208, 9
Rayner J. T., Toomey D. W., Onaka P. M., Denault A. J., Stahlberger W. E., Vacca W. D., Cushing M. C., Wang S., 2003, PASP, 115, 362
Rieke G. H. et al., 2004, ApJS, 154, 25
Rucinski S. M., 2012, in Richards M. T., Hubeny I., eds, Proc. IAU Symp. 282, From Interacting Binaries to Exoplanets: Essential Modeling Tools. Tatranská Lomnica, p. 365–370
Schechter P. L., Mateo M., Saha A., 1993, PASP, 105, 1342
Schlafly E. F. et al., 2018, ApJS, 234, 39
Semkov E. H., Peneva S. P., Munari U., Milani A., Valisa P., 2010, A&A, 523, L3
Semkov E. H., Peneva S. P., Ibryamov S. I., 2017, Bulg. Astron. J., 26, 57
Shappee B. J. et al., 2014, ApJ, 788, 48
Sheinis A. I., Bolte M., Epps H. W., Kibrick R. I., Miller J. S., Radovan M. V., Bigelow B. C., Sutin B. M., 2002, PASP, 114, 851
Sicilia-Aguilar A. et al., 2017, A&A, 607, A127
Siess L., Dufour E., Forestini M., 2000, A&A, 358, 593
Simpson R. J. et al., 2012, MNRAS, 424, 2442
Siwak M. et al., 2016, MNRAS, 456, 3972
Siwak M. et al., 2018a, MNRAS, 478, 758
Siwak M. et al., 2018b, A&A, 618, A79
Siwak M., Dróżdż M., Gut K., Winiarski M., Ogłoza W., Stachowski G., 2019, Acta Astron., 69, 227
Siwak M., Ogłoza W., Krzesiński J., 2020, A&A, 644, A135
Skrutskie M. F. et al., 2006, AJ, 131, 1163
Smette A. et al., 2015, A&A, 576, A77
Smith L. C. et al., 2018, MNRAS, 474, 1826
Stetson P. B., 1987, PASP, 99, 191
Sutherland W. et al., 2015, A&A, 575, A25
Szabó Z. M. et al., 2021, ApJ, 917, 80
Szabó Z. M. et al., 2022, ApJ, 936, 64
Szegedi-Elek E. et al., 2020, ApJ, 899, 130
Udalski A., Szymański M. K., Szymański G., 2015, Acta Astron., 65, 1
Werner M. W. et al., 2004, ApJS, 154, 1
Wiebe D. S., Molyarova T. S., V. A. V., Vorobyov E. I., Semenov D. A., 2019, MNRAS, 485, 1843
Wright E. L. et al., 2010, AJ, 140, 1868
Wu Y. W. et al., 2014, A&A, 566, A17
Zhu Z., Hartmann L., Calvet N., Hernandez J., Muzerolle J., Tannirkulam A.-K., 2007, ApJ, 669, 483

This paper has been typeset from a TEX/LATEX file prepared by the author.